RESEARCH ARTICLE

Key Points:
- Extreme reductions in proxy measurements of electron flux observed by MEX within illuminated induced magnetosphere
- Electron holes distributed near or over regions of significant crustal magnetic field magnitude
- At higher altitudes more events occur over regions of larger model crustal magnetic field magnitude

Correspondence to:
B. E. S. Hall,
besh1@leicester.ac.uk

A survey of superthermal electron flux depressions, or "electron holes," within the illuminated Martian induced magnetosphere

B. E. S. Hall[1], M. Lester[1], J. D. Nichols[1], B. Sánchez-Cano[1], D. J. Andrews[2], H. J. Opgenoorth[2], and M. Fränz[3]

[1]Radio and Space Plasma Physics Group, Department of Physics and Astronomy, University of Leicester, Leicester, UK, [2]Swedish Institute of Space Physics, Uppsala, Sweden, [3]Max Planck Institute for Solar System Research, Göttingen, Germany

Abstract Since Mars lacks a global intrinsic magnetic field, the solar wind interacts directly with the Martian upper atmosphere and ionosphere. The presence of localized intense remnant crustal magnetic fields adds to this interaction, making the Martian plasma system a unique environment within the solar system. Rapid reductions in the electron flux, referred to as "electron holes," occur within the Martian induced magnetosphere (IM). We present a statistical analysis of this phenomenon identified from proxy measurements of the electron flux derived from measurements by the Analyser of Space Plasmas and Energetic Neutral Atoms Electron Spectrometer experiment on board the Mars Express (MEX) spacecraft. The study is completed for the period of 9 February 2004 to 9 May 2014. Electron holes are observed within the IM in more than 56% of MEX orbits during this study period, occurring predominantly at altitudes less than 1300 km, with the majority in the negative X Mars-Centric Solar Orbital direction. The spatial distribution above the surface of Mars is observed to bear close resemblance to that of the crustal magnetic fields as predicted by the *Cain et al.* [2003] magnetic field model, suggesting that they play an important role in the formation of these phenomena.

1. Introduction

Mars lacks an intrinsic global magnetic field, so it is the Martian upper atmosphere and ionosphere that interact directly with the solar wind and interplanetary magnetic field (IMF). This interaction is commonly referred to as "Venus like" [*Cloutier et al.*, 1999], but the presence of localized remnant crustal magnetic fields [*Acuña et al.*, 1998, 1999, 2001] can affect the solar wind interaction in ways not included in the Venus-like description [*Acuña et al.*, 1999; *Edberg et al.*, 2008]. Missions such as the NASA Mars Global Surveyor (MGS, 1996–2006) spacecraft and the European Space Agency (ESA) Mars Express (MEX, 2003 up to present) spacecraft have been used for almost two decades to characterize the intricacies of the Martian plasma system. During this time, variations have been observed in measurements of quantities such as the electron flux and derived plasma moments [e.g., *Mitchell et al.*, 2001; *Soobiah et al.*, 2006; *Brain et al.*, 2007; *Duru et al.*, 2011], as well as apparent large-scale changes in the structure of the ionosphere associated with the crustal magnetic fields [e.g., *Lundin et al.*, 2011; *Nilsson et al.*, 2011; *Andrews et al.*, 2013, 2014; *Dubinin et al.*, 2012].

These phenomena have been classified in previous work at Mars and Venus as rapid reductions in electron flux measurements called "plasma voids" [e.g., *Mitchell et al.*, 2001], while, reductions in the electron number density are called "density depressions" [e.g., *Brace et al.*, 1982]. Although a priori, both classifications could seem similar, it is important to note that particle detectors that make electron flux measurements typically sample superthermal electron populations (>10 eV), whereas instruments responsible for measurements of electron number densities sample across thermal (<10 eV) and superthermal electron populations. Since the number density of the superthermal populations is usually orders of magnitude less than thermal components within atmospheric plasmas, a reduction in electron flux measurements may not always have a corresponding reduction in number density measurements, or alternatively, a so-called plasma void may not have a corresponding density depression. Thus, the description of the phenomenon is highly influenced by the nature of the measuring instrument.

On a global scale, Mars and Venus interact with the solar wind in a similar way, thus it is likely that the aforementioned phenomena at both planets have several similarities. At Venus, *Brace et al.* [1982] identified "ionospheric density holes," deep troughs in the Venusian nightside ionospheric electron density, and found

them to occur in pairs (one in each hemisphere) over regions of strong induced radial magnetic field. The ionospheric holes were suggested to be a possible atmospheric escape route. *Pérez-de-Tejada* [2004] later suggested that the ionospheric density holes are actually large-scale eroded plasma channels in the nightside polar upper ionosphere that extend further from the midnight plane with increased solar wind dynamic pressure. A more recent study by *Collinson et al.* [2014] provided a counter suggestion that discarded the *Pérez-de-Tejada* [2004] mechanism. In this study Collinson et al. proposed that the ionospheric density holes are due to an underlying phenomenon in which a pair of tubes of enhanced draped IMF emerge from below the ionosphere and extend into the Venusian tail. This could then provide a magnetic channel for plasma to escape along the induced field lines leading to the formation of the holes. Despite any similarities between phenomena observed at Venus and Mars, one major distinction that should be noted is the difference in the ratio of ion gyroradius as compared to the planet size. This ratio is typically much larger at Mars than at Venus, thus requiring careful consideration of the processes that could be possible.

In the case of Mars, reductions in electron flux toward background levels, plasma voids, were identified in the Martian optical shadow by *Mitchell et al.* [2001] and were found to occur over regions of crustal magnetic fields. *Mitchell et al.* [2001] suggested that "magnetic cylinders" protruding from highly elongated crustal sources act to restrict the solar wind plasma flow into the magnetotail, whereas on the dayside they fill with ionospheric photoelectrons. Within a void, spikes in the electron flux were attributed to occur when the radial component of the magnetic field was near the local maximum. *Soobiah et al.* [2006] also identified nightside plasma voids along with dayside intensifications in the electron flux. The study was limited to 144 MEX orbits at altitudes close to periapsis, and the identified void/intensification locations were found to coexist with model crustal magnetic field regions [*Cain et al.*, 2003]. *Soobiah et al.* [2006] suggested that the phenomena were related to regions in which strong crustal fields reconnect with the IMF leading to possible atmospheric loss channels.

An indirect study of plasma voids by *Brain et al.* [2007] looked at 7 years of magnetic field and electron flux (energies of 115 eV) measurements by the MGS magnetometer (MAG) and Electron Reflectometer (ER) [*Acuña et al.*, 1992] instruments, respectively. *Brain et al.* [2007] looked at such data to determine the distribution of different types of electron pitch angle distributions (PADs) across the surface of Mars. During the study period, MGS orbited Mars in an almost circular orbit of altitude ~ 400 km, while sustaining a local time orbit of 2 A.M. and 2 P.M. *Brain et al.* [2007] identified plasma voids to have PADs in which the electron flux was effectively at background levels across all pitch angles. Considering the sunlit ($<$90° of solar zenith angle), and dark ($>$120° of solar zenith angle at 400 km altitude) parts of the MGS orbit separately, they found plasma voids to occupy approximately one third (31.5%) of electron PADs when in darkness, but virtually never ($<$7000 out of 31 million PADs) in the sunlit region of Mars. The plasma voids in the eclipse of Mars were identified to be distributed over regions of crustal magnetic fields, with 100% plasma void occurrence (across the full 7 year data set) over the strongest crustal field regions in the Southern Hemisphere. They suggested that these regions were closed crustal magnetic field regions that would remain closed irrespective of external conditions. When in sunlight, these closed field regions were found to be filled with isotropic electron PADs. From this, *Brain et al.* [2007] suggested that when in sunlight plasma source processes would dominate loss processes, but when in darkness, the opposite would be true with removal through atmospheric absorption, scattering into pitch angles where the former can occur, and diffusion away from the closed field regions. Further to this, in the vicinity of closed field regions, PADs corresponding to two-sided loss cones were identified when MGS was in eclipse and were hypothesized to be filled by superthermal electrons through source processes such as reconnection between open crustal fields and the solar wind/IMF, and/or cross-field diffusion.

A study by *Duru et al.* [2011] investigated variations seen in the local nightside ionospheric electron density. Steep electron density gradients and electron density depressions were found, and the authors suggested that these phenomena could be similar to those observed at Venus by *Brace et al.* [1982]. Of the 66 MEX orbits that were studied by *Duru et al.* [2011], steep electron density gradients were observed in 10 (15%) of the orbits, and depressions in 21 (32%) of the orbits. They also presented multi-instrument measurements of electron density (thermal population) and electron flux (superthermal population) across a density depression. They found that the electron flux reduced in 19 cases of density depressions and had no change in a further four depressions. *Duru et al.* [2011] suggested that a density depression joined by a flux reduction might correspond to regions in which the magnetic field is closed, thus restricting the flow of external plasma

into the region. In such a region, sink processes would dominate sources, leading to reductions across all instruments. Cases in which the electron flux has no change across a density depression may occur in closed regions that have sudden access to external plasma, or where atmospheric degradation occurs. Despite the similarity of the density depressions seen at Mars to the ionospheric holes at Venus, one major difference is that the location of events at Venus is in two main regions near the poles, whereas *Duru et al.* [2011] found no convincing evidence of the same distribution at Mars.

More recently, *Steckiewicz et al.* [2015] presented the first results of superthermal electron depletions as observed by multiple instruments on board the NASA Mars Atmosphere and Volatile EvolutioN (MAVEN) mission [*Jakosky et al.*, 2015]. The work by Steckiewicz et al. reported 1742 superthermal electron depletions identified within 3 months of MAVEN orbits. During this time MAVEN was limited to geographic coverage across mid to high northern latitudes but was able to reach low altitudes down to 125 km (nominal periapsis altitude of 150 km) during one of its deep-dip campaigns. The electron depletions were identified within the nightside ionosphere of Mars. Steckiewicz et al. found that the spatial distribution of electron depletions was highly dependent on altitude. Above 170 km they were mainly distributed around and above strong crustal magnetic field regions, whereas, at lower altitudes they were distributed more homogeneously across the surface. They noted a higher probability of depletions in the lower altitude regime, with 46% occurrence probability decreasing to 14% within the higher-altitude regime. The design of the instruments on board MAVEN allowed Steckiewicz et al. to investigate the low-energy distributions within a depletion, which allowed them to suggest that the low-altitude events exist due to electron absorption by CO_2 within the Martian ionosphere.

The objective of this paper is to present a study of rapid reductions in electron flux within the Martian induced magnetosphere (IM) by doing a more exhaustive analysis of the occurrence of such reductions using the MEX Analyser of Space Plasmas and Energetic Neutrals Electron Spectrometer (ASPERA-3 ELS) instrument [*Barabash et al.*, 2006]. The main advantage of this study is the much longer time period that the MEX ELS data set covers as compared to other missions to Mars. In addition to this, the MEX elliptical orbits allow for broader coverage throughout the plasma environment of Mars. Therefore, the study reported here is carried out over a larger time period, consequently leading to better spatial coverage of the Martian plasma environment, as compared to the studies described above. In section 2 we briefly describe the MEX mission, ASPERA-3 ELS instrument, and the derived electron flux proxy study data set (see section 2.1). Within the same section we also describe the automated method for identification of electron flux reductions (see section 2.2), as well as a sensitivity analysis done on the algorithm (see section 2.3). In section 3 we present the statistical results related to the occurrence and locations of electron flux reductions identified across the study period, and finally, in sections 4 and 5 we discuss and conclude upon these results. Henceforth, the electron flux reductions will be referred to as "electron holes."

2. Instrumentation and Observations

2.1. Mars Express, the ASPERA-3 ELS Instrument, and Data Set

In this study we use data obtained by the ESA Mars Express ASPERA-3 ELS instrument [*Barabash et al.*, 2004, 2006]. Science operations of MEX started in January 2004, with the spacecraft placed into an elliptical orbit with average periapsis and apoapsis at 287 km and 11560 km, respectively [*Chicarro et al.*, 2004]. The mission was designed to give MEX a latitudinal shift in periapsis location over time such that global coverage of the surface can be achieved [*Pischel and Zegers*, 2009]. The ASPERA-3 ELS instrument is able to measure electrons within the energy range of 1 eV–20 keV [*Frahm et al.*, 2006] and has an energy resolution of 8%. The instrument operates by collimating particles within an intrinsic field of view (FOV) of 4° × 360° into a spherical top-hat electrostatic analyzer. The detector comprises 16 anodes each defining a 22.5° sector of the FOV. The spectrometer samples particles over the above energy range by stepping a positively charged deflection plate through a range of voltages. ASPERA-3, and thus ELS, is situated on a scanning platform (first activated in 2006, 2 years after orbit insertion) that allows for full 4π angular distribution measurements of electrons with a selectable scan time of 32, 64, or 128 s.

The above describes the overall operational capabilities of ASPERA-3 ELS. However, the instrument was designed to be flexible, allowing for multiple operational modes (e.g., energy range and measurement cadence). In general, however, ELS has been operated in the four following modes: (1) Default/Survey mode,

full energy range across 128 log-spaced energy steps with a 4 s cadence. (2) Linear mode, reduced energy range of 1–127 eV across 128 linearly spaced energy steps, also with a 4 s cadence. (3) The 1 s mode, reduced energy range of 10–160 eV across 32 log-spaced energy steps with a 1 s cadence. (4) The 32 Hz mode, single energy channel (variable energy), with a cadence of 32 Hz.

The first two of these modes are detailed in *Frahm et al.* [2006]. The default mode (mode 1, survey) is most commonly used, operating >96% during the time interval of this study. The linear mode (mode 2) is utilized about once a month (~1% of the study interval), while the 32 Hz mode (mode 4) is rarely used. The 1 s mode (mode 3) is used more sporadically but when operated tends to last for several orbits in sequence (~2% of the study interval). Due to the way ELS is operated, for an individual MEX orbit, the mode is kept the same throughout the entire passage of the Martian IM.

For this study, a proxy of the ELS measurements of the electron flux (differential number flux, DNF) is created, henceforth called the f parameter. This is calculated by integrating the DNF over the energy range of 20–200 eV. Since several of the ELS modes do not cover this full energy range, and in the case of the linear mode (mode 2), undersampling and oversampling of the DNF become significant [*Frahm et al.*, 2006], this study only includes measurements by ELS when operating in Survey mode (mode 1). The detailed process for calculating the f parameter is as follows. For each full energy scan of ELS (i.e., every 4 s in survey mode), the average central energies that are sampled are calculated from all 16 anode sectors of the ELS detector (ELS central energy is slightly anode dependent, see *Frahm et al.* [2006]). The average DNF per steradian (units of electrons $cm^{-2} s^{-1} sr^{-1} eV^{-1}$) for each average central energy is then calculated by also taking the average measured DNF across all 16 anode sectors. Since each anode sector has equal FOV the above gives us an isotropic energy spectrum of the DNF. Next, we integrate the DNF into an energy range of 20–200 eV by summing over all energy channels within this range and multiplying by the total energy range (180 eV). Finally, we assume that this value is representative of the full 4π coverage and multiply by 4π. This process gives us a proxy measurement of the DNF, i.e., the f parameter (units of electrons $cm^{-2} s^{-1}$). This process neglects the effects of contamination from sources such as rediffused and secondary electrons for anodes of ELS that look across the spacecraft body. We discuss the impacts of such contamination later in this section.

There are multiple caveats involved when considering particle detectors. For ELS these include (1) variable spacecraft charging, (2) FOV restrictions, and (3) contamination which we now discuss in turn. The net charge of a spacecraft can dramatically impact the distributions measured by charged particle instruments. A negative spacecraft potential would act to deflect negatively charged ions and electrons away from the detector, thus shifting the observed species to lower energies of the energy spectrograms, possibly completely restricting their observation. A positive spacecraft potential would have the opposite effect, accelerating negatively charged species to higher energies. Throughout the MEX passage of the Martian system, the spacecraft potential varies, typically being negatively charged when passing through the Martian ionosphere and IM [*Fränz et al.*, 2007]. Our choice of an energy integration range of 20–200 eV when calculating the f parameter (see above) was set in an attempt to negate spacecraft charging effects. In general, it is charged particles of lower energies (e.g., thermal) that are most sensitive to spacecraft charging, thus the lower limit of 20 eV was chosen. The upper limit of 200 eV was set since electron fluxes above this are typically several orders of magnitude lower than within the 20–200 eV range (see Figure 2). Thus, the 20–200 eV integration range covers the breadth of energies generally seen within the Martian IM.

The ASPERA-3 ELS instrument is comprised of 16 anode sectors, each with the same FOV, but certain anodes can have parts of the MEX spacecraft body within its FOV (see *Frahm et al.* [2006] for details). This leads to restrictions in certain anodes not being able to sample the full parent population of electrons across its entire FOV. In addition to this, ELS is situated on a scanning platform (first activated in 2006). As the scanner, and consequently ELS, rotates the specific anodes that view across the spacecraft body vary. Throughout a passage of the Martian IM, the ELS scanner position remains constant. Therefore, any distortion in measurements of the DNF for blocked anodes is consistent throughout the entire passage.

In addition to reduced DNF measurements for FOV-restricted anodes, the same anodes may also measure contaminated signals. These contaminated signals arise from measurements of photoelectrons (driven by UV radiation) and reflected, rediffused, or secondary electrons (driven by electron impact), all from the spacecraft surface. Photoelectrons are typically emitted at energies below 20 eV, thus they should be negated by our calculation of the f parameter. Reflected and rediffused electrons can have energies

anywhere up to just below the incident energy of the electron impacting the spacecraft surface, whereas secondary electrons can have energies up to 50 eV [*Furman and Pivi*, 2002] for high-energy electrons impacting the surface (less common within IM). These sources of contamination can distort the spectrum measured by anodes viewing across the spacecraft body. By taking the average DNF across all anodes when calculating the *f* parameter, we expect these contamination effects to not have a significant impact on our proxy measurement of the electron flux. In addition, we also expect that the levels of contamination to be consistent throughout the passage of the illuminated Martian IM. We do note that, other than averaging across all ELS anodes, irrespective of their FOV restrictions, no further processing has been implemented to reduce/remove contaminated signals. Other sources of contamination due to (1) changes in the background UV entering detector, (2) changes in background penetrating radiation, and (3) saturation of the sensor are more likely to be anode independent, thus distorting the entire spectrum. Sources (2) and (3) are usually related to solar energetic particle and coronal mass ejection events; both of which are expected to be uncommon throughout the data set and an altogether different topic in identifying when they occur. Due to this, no attempt was made to remove these three sources of contamination. Due to our processing of the DNF not fully accounting for all sources of contamination, we note that our *f* parameter is a proxy measurement of the true electron flux measured by ELS.

The *f* parameter electron flux proxy data set used in this study spans more than 5 Martian years (~10 Earth years) from 9 February 2004 to 9 May 2014 and contains a total of 13053 MEX orbits, from which 8718 orbits have electron flux proxy data within the illuminated Martian IM useful for this study. The difference in these values are due to 3411 orbits simply having no data available (e.g., instrument was not in operation), 652 orbits having ELS operating outside of the survey mode (mode 1), and the remaining 272 orbits contained no data within the illuminated IM. The data used in this study were obtained from the processed ASPERA-3 ELS data sets available online at the ESA Planetary Science Archive (http://www.rssd.esa.int/psa). Finally, all MEX spacecraft coordinates used in this study are calculated using the NASA SPICE system [*Acton*, 1996].

In Figure 1a we show the spatial distribution of MEX orbits, and in Figure 1b show the mean of the log ASPERA-3 ELS electron flux proxy, *f*, in units of electrons cm^{-2} s^{-1}, for the entire interval of this study. Both panels present the respective data in a cylindrical Mars-Centric Solar Orbital (MSO) coordinate system, where the X_{MSO} coordinate is the abscissa, and the cylindrical radius $\rho_{MSO} = (Y_{MSO}^2 + Z_{MSO}^2)^{1/2}$ is on the ordinate. In the MSO system, +X is directed toward the Sun, +Y is in the opposite direction to Mars' orbital velocity vector (toward dawn) and +Z completes the right-handed set. The spatial bin size is $0.05 \times 0.05\, R_M$ (Martian radius, $1\, R_M \sim 3390$ km). The model bow shock (dash-dotted line) and magnetic pileup boundary (MPB, dashed line) positions from *Edberg et al.* [2008] are also shown. In both panels, a white bin represents no data points available. The saturating range of the color table in Figure 1b was chosen to show good definition of the *f* parameter in each region of the Martian plasma system. With this color selection, the optical shadow (i.e., the region where $\rho < 1$ for $X_{MSO} < 0$), the magnetosheath (region between the bow shock and MPB), and the solar wind (region outside bow shock) are all well illustrated. For simplicity, we refer to the region of space inside the MPB as the Martian IM. The majority of the illuminated IM (the IM outside of the optical shadow) has a similar level of *f*, typically ranging from $\sim 10^{8.8-9.2}$ electrons s^{-1} cm^{-2}. For positive X_{MSO} the evolution in *f* from IM to magnetosheath fluxes is quite significant, rapidly increasing to $\geq 10^{9.5}$ electrons s^{-1} cm^{-2} (yellow-red colors). For negative X_{MSO}, the evolution in *f* is much less evident, with magnetosheath fluxes represented by values exceeding $10^{9.2}$ electrons s^{-1} cm^{-2}. In general, the model MPB and bow shock are consistent with the magnetosheath region on the nightside but do not fit as well toward the subsolar point. With the absence of a method to reliably identify the MPB along each orbit, the *Edberg et al.* [2008] model MPB is taken as a suitable indicator of where the IM begins and ends and, therefore, is used in this study to identify any IM data within a MEX orbit.

2.2. Identification of Electron Holes

The MEX orbit evolves over time such that the spacecraft passes through different regions of the IM. To illustrate this orbital evolution, three different orbital configurations have been selected as representative examples (Figure 2a), and their respective measurements taken by the ASPERA-3 ELS instrument are also shown (Figures 2b–2d). The MEX orbits in Figure 2a are shown in cylindrically symmetric MSO coordinates, and the orbits are approximately one Earth year apart from 2010 to 2012. Orbit 7838 on 12 February 2010 is shown in black, orbit 9143 on 27 February 2011 in blue, and orbit 10392 on 26 February 2012 in red. The bars
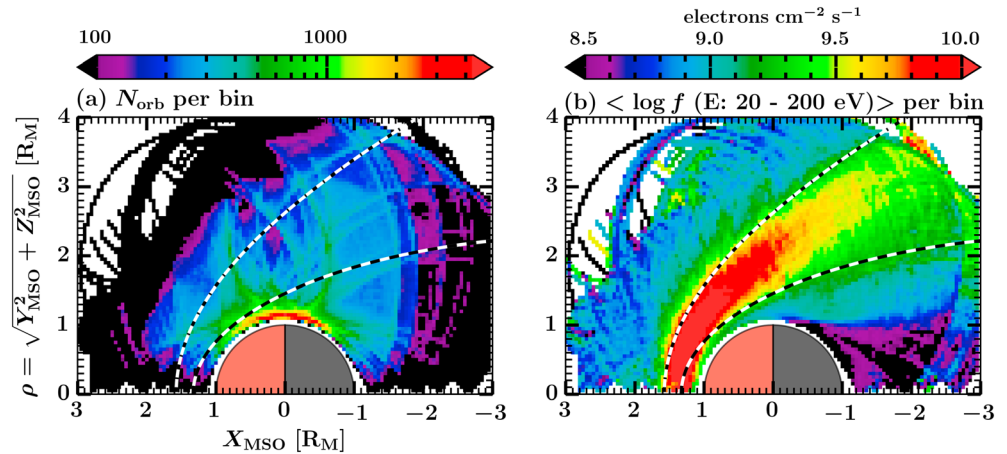
Figure 1. ASPERA-3 ELS data distributions across the period of 9 February 2004 to 9 May 2014 in a Mars-Centric Solar Orbital (MSO) coordinate frame. The MSO coordinate axes are with respect to the Sun-Mars line (X_{MSO}) and the cylindrically symmetric axis ($\rho = (Y_{MSO}^2 + Z_{MSO}^2)^{1/2}$), both in terms of average Mars' radii ($R_M = 3390$ km). Positive X_{MSO} is toward the Sun, with the terminator plane at the $X_{MSO} = 0$ plane. For the conditions of $X_{MSO} < 0$ and $\rho < 1$, regions of space are approximated to being unlit by solar irradiation and thus in the optical shadow of Mars. The spatial resolution of both panels is 0.05×0.05 R_M. (a) Mars Express orbital coverage when ASPERA-3 ELS was in operation. Less than 100 orbits are represented by black bins. (b) Distribution of mean log electron flux proxy, f (energy range: 20–200 eV), in units of electrons cm^{-2} s^{-1}. Values of less than $10^{8.5}$ electrons cm^{-2} s^{-1} are represented by black bins. Saturation is shown above 10^{10} electrons cm^{-2} s^{-1} by red bins. In both panels, white bins show no data coverage, and the *Edberg et al.* [2008] model bow shock (dash-dotted line) and magnetic pileup boundary (dashed line) locations are superimposed for further context.

on each orbit track represent the start/end of observations shown in Figures 2b–2d. The model bow shock and MPB positions [*Edberg et al.*, 2008] are shown as dash-dotted and dashed lines, respectively. For each of the orbits, MEX is in the solar wind at apoapsis and travels into the postterminator ($X_{MSO} < 0$) side of the Martian IM after passing through the bow shock, magnetosheath, MPB, and then continuing to periapsis, which also evolves in position between orbits. MEX then passes through these boundaries/regions in reverse order back toward apoapsis in the solar wind. Periapsis for all orbits across the study period is, on average, around 350 km and varies in position with respect to the day and nightside of Mars. Only one of these sample orbits (orbit 7838, Figure 2b) has an excursion into the optical shadow, identified as a pink profile segment in Figure 2a and the f parameter profile in Figure 2b.

The ASPERA-3 ELS data available for the period of the orbits 7838, 9143, 10392 are shown in Figures 2b–2d, respectively. For each orbit/panel, the ASPERA-3 ELS electron spectrum averaged across all anodes of the detector is shown for the full range of measured energies. The colors of the electron spectra represent the log differential number flux (DNF) of electrons incident on the detector in units of electrons cm^{-2} s^{-1} sr^{-1} eV^{-1} with the range shown in the colorbar. Superimposed on each ELS spectra is the derived electron flux proxy, the f parameter (see section 2.1 for details). The left-hand y axis corresponds to the ELS spectra electron energies (eV), whereas the right-hand corresponds to f and is in units of electrons cm^{-2} s^{-1}. The ELS spectra and f profile both share a common timescale (x axis). The f profile has undergone further processing to reduce high-frequency variations by utilizing a rolling median filter of window size 16 s. Also overlaid upon the ELS spectra are the *Edberg et al.* [2008] model bow shock crossings, shown by the two outermost (inbound/outbound crossing) solid vertical black lines, and the *Edberg et al.* [2008] model MPB crossings, shown by the two innermost solid vertical black lines. The median and lower quartile of the f parameter within the IM (e.g., data bound by in and outbound model MPB crossings) have been calculated for the identification of electron holes (described later in this section) and are overlaid as solid and dashed horizontal red lines, respectively. For each ELS spectrum in Figure 2, the position of MEX in terms of altitude (km) and solar zenith angle (SZA, degrees) is also given on the x axis.

Orbit 9143 (Figure 2c) shows the most pronounced changes in electron flux when MEX transitions between different regions of the Mars' plasma environment and is now described in detail with the other orbits sharing a similar interpretation. MEX is in the solar wind until ~17:35 UT when a rapid enhancement in the electron DNF is observed across all energies indicating a pass through the bow shock into the magnetosheath. The
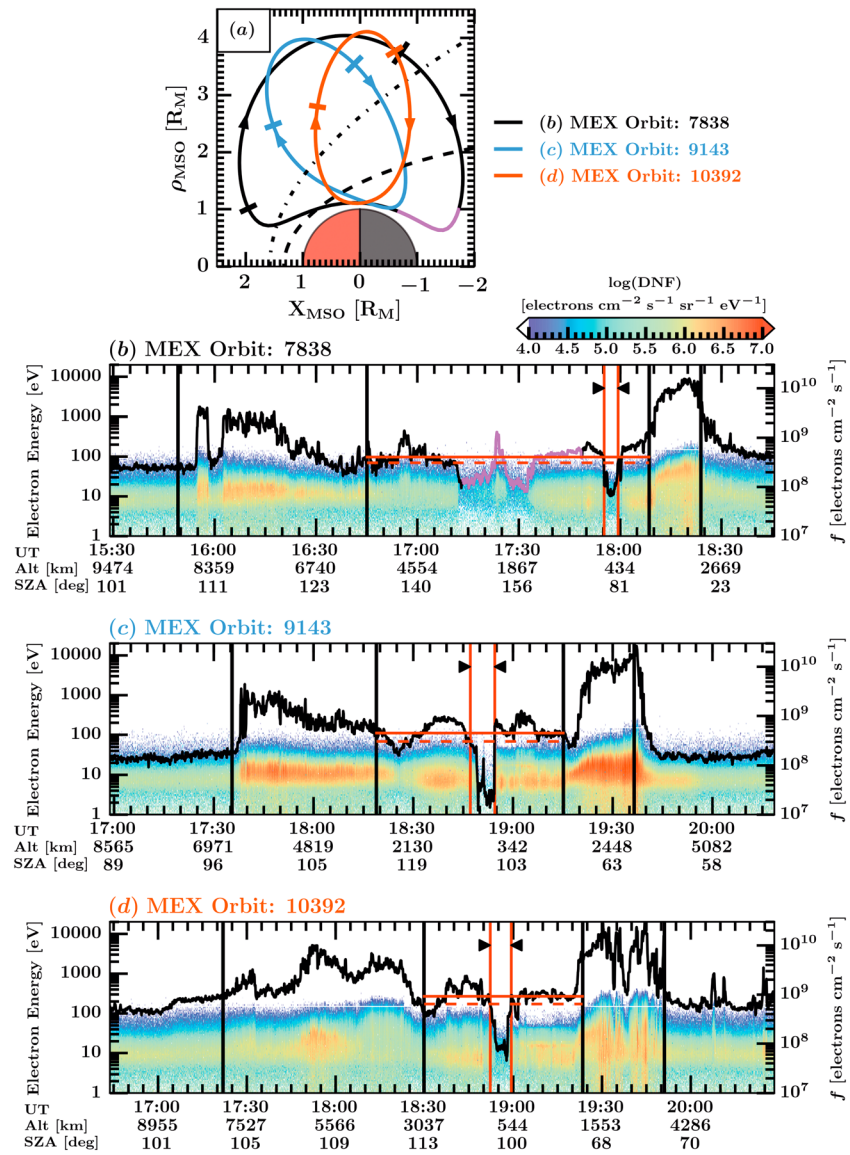
Figure 2. Observations of electron hole phenomena in three sample MEX orbits across the time period of 1 January 2010 to 30 April 2012. (a) MEX orbital trajectory for orbits 7838 on 12 February 2010 (black), 9143 on 27 February 2011 (blue), and 10392 on 26 February 2012 (red), all in a cylindrically symmetric MSO coordinate frame (both axes in terms of Martian radius). The *Edberg et al.* [2008] model bow shock (dash-dotted line) and MPB (dashed line) positions are given for further context. The horizontal bars represent start/end data acquisition by ASPERA-3 ELS shown in further panels. Pink orbit segment represents passage into Martian optical shadow. (b–d, left axis) ASPERA-3 ELS electron energy spectra for MEX orbits 7838, 9143, and 10392, respectively. The colors correspond to the electron Differential Number Flux (DNF, electrons $cm^{-2} s^{-1} sr^{-1} eV^{-1}$), with lower limit at DNF $< 10^4$ (white) and saturation limit at DNF $\geq 10^7$ (red). (right axis) The electron flux proxy, *f*, (based on the electron DNF integrated across the energy range of 20–200 eV and in units of electrons $cm^{-2} s^{-1}$) for each orbit is superimposed (black profile) on each panel sharing the common timescale. Also in each panel are the points MEX crosses the *Edberg et al.* [2008] model bow shock and MPB locations, shown by the outer and inner pair of solid vertical black lines as the spacecraft enters the Mars system and in reverse order of appearance upon exiting the Mars system. The electron spectra and *f* parameter profiles all show variations that are referred to in the text. The reduction highlighted by a pink profile in Figure 2b corresponds to MEX entering the optical shadow of Mars. Significant reductions outside of the optical shadow correspond to electron holes and are marked by solid vertical red lines (enclosed by black arrowheads). The median and 25th percentile values of the *f* parameter within the illuminated IM are overlaid as horizontal red solid and dashed lines, respectively. The MEX altitude and solar zenith angle (SZA) of MEX is given for each timestamp.

model bow shock position is identified at a similar time. The enhancement lasts until ~18:20 UT when the DNF reduces. This latter boundary is likely the MPB, as evidenced by a crossing of the model location at a similar time. Similar features are seen at ~19:20 and 19:40 UT corresponding to dayside crossings of the same boundaries but in reverse (the model crossings of MPB and bow shock are at ~19:15 and ~19:35 UT, respectively). The region between the inbound and outbound model MPB crossings is interpreted as the Martian IM. As seen in the electron spectra of Figures 2b and 2d, nightside crossings of the bow shock and MPB are not always easily identifiable. Figure 1b demonstrated that the edges of the magnetosheath region were consistent with the *Edberg et al.* [2008] model boundary positions. In addition to this, the dayside model boundaries are a good match to enhancements in the electron flux spectra as seen in Figure 2. Thus, the model MPB positions are confirmed as suitable estimates for identifying when MEX is within the Martian IM.

As mentioned previously, the orbit in Figure 2b includes a transition into the optical shadow of Mars between ~17:10 and ~17:50 UT (highlighted in the *f* parameter profile as a pink segment). During this period in the optical shadow, a plasma void (along with an enhancement during the void) as described by *Mitchell et al.* [2001] may be present. In general, the *f* parameter distribution shown in Figure 1b shows that the optical shadow of Mars is host to fluxes significantly lower than those seen in the illuminated IM.

The electron holes are defined as significant reductions in the electron flux from average levels of flux across a wide range of energies within the illuminated Martian IM. The electron holes identified in the three examples in Figure 2 occur between the red vertical lines at the times 17:55–~18:00 UT of orbit 7838 (Figure 2b), ~18:45–18:55 UT of orbit 9143 (Figure 2c), and ~18:50–~19:00 UT of orbit 10392 (Figure 2d). The electron holes were identified using an automated algorithm (see next paragraph for details) and the derived *f* parameter electron flux proxy, which includes electron fluxes across the energy range of 20–200 eV. A significant reduction across the 20–200 eV range shows an absence of electrons rather than a shift in the population due to spacecraft potential effects. Comparison of the *f* parameter profiles with the electron spectra for the same time period (see Figures 2b–2d) shows that the integration range of 20–200 eV, and *f* parameter itself, gives a good representation of the variations seen in DNF across a wide range of energies of the ELS spectra. As mentioned before, the *Edberg et al.* [2008] model MPB locations were used to identify when MEX was within the Martian IM. As seen in Figures 1b and 2b, the optical shadow of Mars typically contains electron flux populations significantly different from the illuminated atmosphere. In order to differentiate these events from those discussed previously by *Mitchell et al.* [2001], *Soobiah et al.* [2006], *Brain et al.* [2007], and *Steckiewicz et al.* [2015], this study only considers electron holes outside of the optical shadow.

The automated algorithm used in this study is described in the following process. For each MEX orbit, the typical range of *f* (and thus variation) was taken as those that fall within the boundaries of the interquartile range of *f*, calculated from measurements within the illuminated IM. An electron hole was then identified when the following criteria were met:

1. The *f* parameter must reduce below the lower quartile (25th percentile) value of *f* within the illuminated IM (dashed horizontal red lines in Figures 2b–2d), marking the start of a potential electron hole, while the end of the hole occurs when *f* increases back above the 25th percentile.
2. The reduction below the 25th percentile must last longer than 12 s, thereby reducing statistical variation.
3. The minimum *f* during the reduction must be at least a half an order of magnitude reduction from the median proxy flux within the IM calculated for that orbit (solid horizontal red lines Figures 2b–2d).

The choice of thresholds in criteria (1), (2), and (3) was chosen to reduce a large proportion of false positive identifications, as demonstrated by the Sensitivity Analysis in section 2.3. Events that have not met criteria (2) and (3) can be seen in all *f* profiles of Figure 2, with multiple short deviations below the lower quartile value (dashed horizontal red line), e.g., at around 16:45–16:55 UT of orbit 7838 (Figure 2b), and deviations that do not exceed a half magnitude reduction from the median *f* value (solid horizontal red line) at, e.g., ~18:20–18:30 UT of orbit 9143 (Figure 2c), and ~19:00–~19:05 UT of orbit 10392 (Figure 2d). Events that meet these criteria are shown in Figures 2b–2d with vertical red lines identifying the start and end (enclosed by black arrowheads).

2.3. Sensitivity Analysis of Identification Algorithm

As noted above, the identification algorithm used in this study considers a reduction in the electron flux proxy, *f*, to be an electron hole if it has a minimum duration of 12 s, and at least a half order of magnitude

Table 1. Sensitivity Analysis of Number of Identified Electron Holes Through Small Changes to Identification Algorithm[a]

τ_{min}	Percentile Threshold (%)	N_{hole}	N	P (%) ($N/N_{tot,orb} \times 100$)	N_{hole}/Orbit	$<\tau>$/s	$<w>$/km	$<\Delta>$
12 s	35	7592	4586	53	1.66	332	1192	0.82
	25	9617	4907	56	1.96	210	759	0.80
	15	12596	5323	61	2.37	120	435	0.79
24 s	35	7464	4561	52	1.64	338	1211	0.82
	25	9132	4866	56	1.88	220	795	0.81
	15	11131	5254	60	2.12	133	484	0.81

[a]Where not explicitly stated, values in the table are described in the text in section 2.3

reduction in f from average levels in the illuminated IM (criteria 2 and 3). However, before these criteria are even evaluated, the flux first has to reduce below the 25th percentile value of f within the illuminated IM (criteria 1). A reduction below this initial identification threshold is thus the most important criterion in identifying an event. Two sensitivity checks have been performed. The first varied the initial identification threshold (15th, 25th, and 35th percentiles), and the second varied the minimum allowed time for an event ($\tau_{min} = 12$ s and 24 s). For these two sensitivity checks, the number of electron holes found, N_{hole}, the number of corresponding MEX orbits from which the holes were identified, N, and the average (mean) values of parameters such as duration, $<\tau>$, width, $<w>$, and depth, $<\Delta>$ of the holes are shown in Table 1. The width of an electron hole is calculated using the same method as used by *Duru et al.* [2011] for density depressions, which takes into account the MEX altitude change, and length of MEX passage across the region, and thus is a measure of the scale size of the hole. The electron hole depth was calculated as the order of magnitude reduction at the lowest point across a hole from the empirically calculated median integrated flux within the illuminated IM of each orbit. Moreover, in Table 1 we include the probability (as a percentage) of an orbit containing at least one electron hole ($P = N/N_{tot,orb}$) and the effective number of holes per orbit for each case.

Note that the probability of an orbit having a hole, P, changes only by a maximum of 1% when τ_{min} is increased, and there is only a maximum difference of 5% between each identification threshold. For both cases of τ_{min}, the number of holes and the number of orbits with at least one hole increases as the identification threshold decreases. This gives an immediate impression that the lower our initial identification criterion, the more holes are found. However, as seen in the ratio between N_{hole} and N, the reality is that there are more holes per orbit rather than new orbits with holes in them. To illustrate this, in Figure 3 we present a schematic diagram of a reduction in the f parameter. The f profile (black line with red, blue, and green segments) is viewed as representative f within the illuminated IM, with the average (median and 50th percentile) f represented by a solid horizontal blue line corresponding to the same quantity plotted in Figures 2b–2d (red solid). The red, blue, and green horizontal dashed lines correspond to initial identification thresholds of the 35th, 25th, and 15th percentiles, respectively. The region in which a hole or multiple holes may be identified is shown in the figure. This schematic aims to show that the electron holes do not always have a regular trough-like shape (as seen with the event commencing at ~18:50 UT in Figure 2d) but can also have variability in f within a hole region (as seen within the event commencing at ~18:45 UT in Figure 2b). Considering the schematic in Figure 3, when taking the 25th percentile (blue dashed horizontal line) we find two holes. If
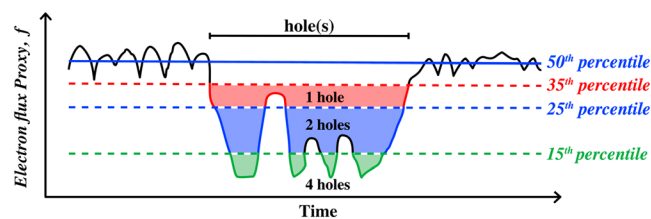

Figure 3. Schematic diagram showing possibility of multiple electron holes being identified within the same depressed electron flux proxy region dependent on choice of initial identification threshold. The electron flux proxy, f, is represented by the black profile, with red, blue, and green segments. The label "hole(s)" denotes a depressed f region. The blue horizontal solid (median and 50th percentile f) and dashed (lower quartile f and 25th percentile) lines are the same as those described in Figure 2 and the text. Other dashed horizontal lines represent different initial identification thresholds for electron holes and are set at the 35th percentile (red) and 15th percentile (green). Regions in which the initial identification thresholds intersect the f parameter profile are shaded in the same color as the threshold to show the impact on multiple holes being identified dependent on threshold chosen.

we then increase the identification threshold by 10% (35th percentile, red dashed horizontal line), we find only one hole of longer duration, which will also correspond to a larger spatial size. Reducing the identification threshold by 10% (15th percentile, green dashed horizontal line), we now find four individual holes each of much shorter durations and thus spatial size. Thus, a differing number of holes can be identified within the same region depending on the identification threshold used. From this, a lower identification threshold (i.e., 15th percentile) is more sensitive to small increases in flux within a flux reduction, leading to more electron holes being identified, and thus an increase in false identifications. To mitigate this possibility, a higher identification threshold can be set. However, if the threshold is set too high (i.e., 35th percentile), some real events can be missed. This also may have the impact of artificially extending the duration of an event, which in turn leads to difficulty in correctly identifying the region of space in which the hole occurred.

In conclusion, after taking into account the small difference in P, and the sensitivity analysis described above, we consider that an identification threshold set at the 25th percentile value and a minimum time criterion of $\tau_{min} = 12$ s are appropriately set for this study.

As noted previously, the *Edberg et al.* [2008] model MPB locations have been used in this study to identify where the Martian IM starts and ends. The average (median) of the f parameter within the illuminated IM is then calculated and used in criterion 2 to identify the electron holes. It is thus expected that the choice of start and end of IM will impact the average value calculated. Although no sensitivity analysis has been completed with respect to this, the expected impact is described here. If the model MPB boundaries are such that magnetosheath data are included in our classification of IM data, we expect the average electron flux proxy within the IM to increase. The percentile threshold calculated for criterion 2 would also increase. As in the sensitivity analysis above, when the percentile threshold is increased, the number of holes identified decreases (Figure 3). Despite this, by using the median as an average, including a small amount of extra values of high f is not expected to change the median value by a great amount. Now, if we consider the opposite case in that the model MPB locations are positioned so we lose valid IM data, our average flux is even less likely to change by a significant amount. However, we are losing valid data, so there is a possibility of missing valid electron hole identifications. In general, for both of the above cases, we expect that the number of identified electron holes to reduce, although, due to the large data set being used in this study, we do not expect the impact to be statistically significant.

3. Statistical Results

During the time period of 9 February 2004 to 9 May 2014, MEX completed 13053 orbits of Mars, with 8718 orbits including valid ASPERA-3 ELS data (as described in section 2.1) that could be used to identify the electron hole phenomena. Within 4907 of these orbits a total of 9617 electron holes were identified, that is 56% of orbits in the interval contained at least one electron hole event. When referring to the ephemerides of an event (i.e., altitude, latitude, and longitude) the central point of an event is used. The ephemerides of MEX are obtained using the NASA SPICE system [*Acton*, 1996]. For the cases of geographic coordinates, MEX typically uses east longitude [*Zender et al.*, 2009], and for consistency, we continue this tradition. The central point ephemerides of the electron holes are now presented in terms of distributions of occurrence (section 3.1), altitude with respect to the Sun-Mars line ($\pm X_{MSO}$) (section 3.2), location above the Martian surface and the *Cain et al.* [2003] crustal magnetic fields (section 3.3), and finally, occurrence in altitude above longitudinal regions of the Martian surface (section 3.4).

3.1. Electron Hole Occurrence Distributions

Figure 4 presents the distributions of electron hole altitude, h_{hole}, (Figure 4a), duration, τ_{hole}, (Figure 4b), width, w_{hole}, (Figure 4c), and depth, Δ_{hole}, (Figure 4d). Electron hole altitudes and widths are grouped into spatial bins of 100 km, the durations are grouped into temporal bins of 0.5 min, and finally, the depths are grouped into bins of size 0.05 order of magnitude reduction. The number of observations per bin of all distributions, $N_{obs}(h/\tau/w/\Delta)$, is given on a logarithmic scale to enhance the tail end of the distributions. The green and blue histogram bars together show the distribution of all identified electron holes, whereas the green histogram bars by themselves show each distribution for electron hole events identified at altitudes, $h \leq 1300$ km (the reason for this choice of altitude is discussed later in this section). For each of these distributions the minimum and maximum values are given. For the entirety of the distribution these values are in
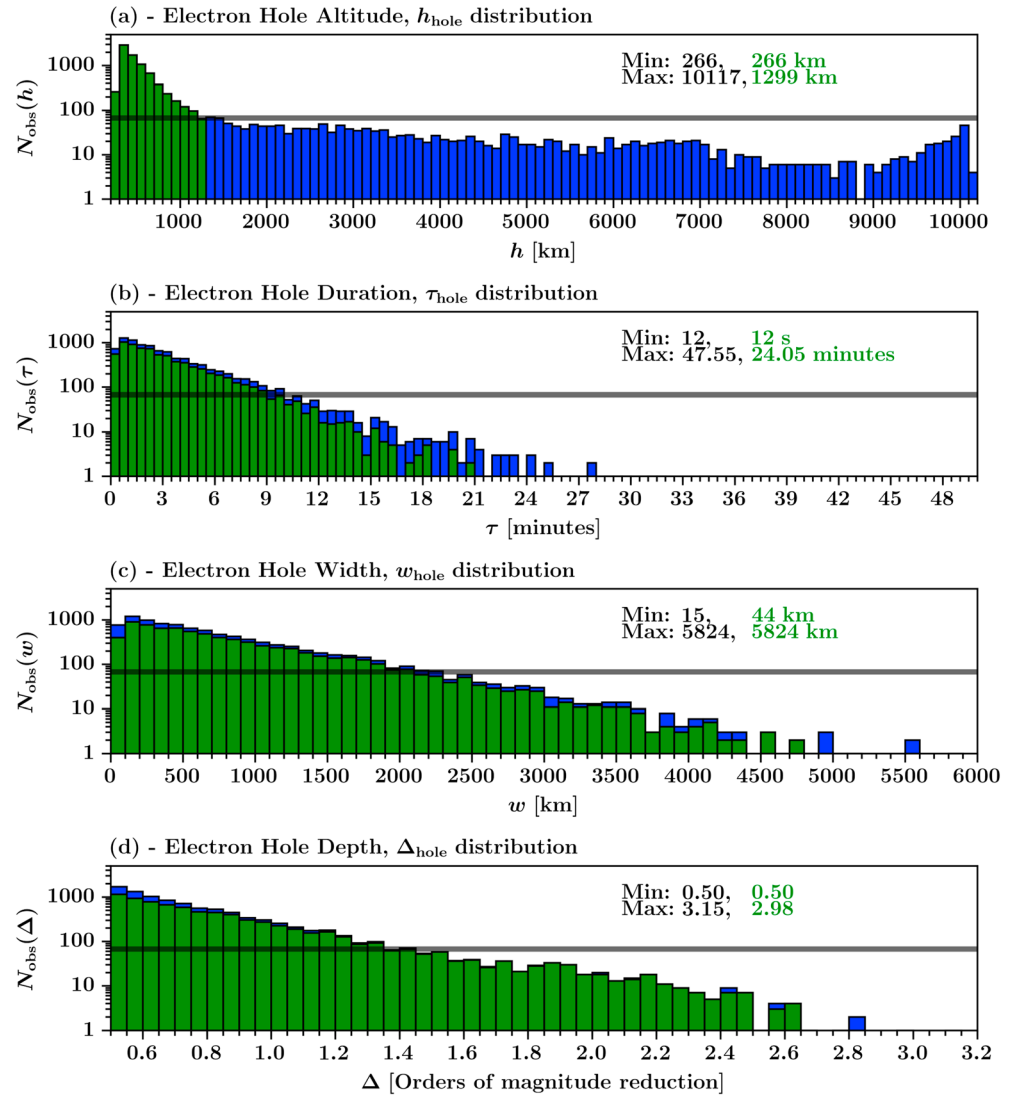
Figure 4. Histogram distributions of electron hole parameters. (a) Altitudes at central point of event, h_{hole}, (b) event durations, τ_{hole}, (c) event width, w_{hole} and (d) depth, Δ_{hole}, of event in terms of orders of magnitude reduction from median electron flux proxy parameter, f, within illuminated IM. All distributions are shown with number of observations per bin N_{obs} (vertical axis) on a logarithmic scale. A solid horizontal black line is overlaid in each distribution representing $N_{obs} = 68$. The altitude, duration, width, and depth distributions have bin sizes of 100 km, 0.5 min, 100 km, and 0.05 respectively. The blue and green histogram bars together represent the full distribution of identified electron holes, whereas the green bars by themselves represent the distributions for only those below altitudes of 1300 km. Also on all distributions are the minimum and maximum values for the full distributions (black text) and for the reduced altitude distributions (green text).

black text, which corresponds to the green and blue bars together, whereas for electron holes at altitudes $h \leq 1300$ km, the values are in green text. Finally, a horizontal black line is overlaid at $N_{obs} < 65$, corresponding to the number of observations in the final altitude bin prior to exceeding $h = 1300$ km.

The maximum number of electron hole observations per altitude bin is $N_{obs}(h) = 2897$ and occurs within the altitude bin of $h = 300$–400 km (Figure 4a). This range is where the MEX periapsis occurs for the majority of the study period. The reduction in occurrence for the altitude bin prior to this is likely an orbital effect since MEX only reached altitudes less than 300 km at the beginning of the mission. From the peak altitude bin, the number of observations per bin reduces at different rates across the whole distribution. We find that ~80% of events occur at altitudes, $h \leq 1300$ km. Up to this altitude, $N_{obs}(h)$ steadily decreases from the peak value with increasing altitude. At altitudes above 1300 km, $N_{obs}(h)$ initially increases slightly and then slowly reduces from $N_{obs}(h) = 70$ to $N_{obs}(h) \sim 20$ at $h = 5200$ km. Above this altitude, $N_{obs}(h)$ varies between 1 and 20 observations per bin

until an altitude of 9500 km is reached. Above this altitude, there is a slight upward trend with a small peak of $N_{obs}(h) = 46$ at $h = 10000$–10100 km. Within the IM, such high altitudes can only be reached by MEX as it approaches apoapsis, placing the holes within the induced magnetotail, and likely close to the model MPB location. We therefore believe this represents an artificial peak due to the orbital configuration and the presence of tenuous plasma populations in this region.

The maximum number of electron hole observations per duration bin is $N_{obs}(\tau) = 1284$, in the period $\tau = 0.5$–1.0 min (Figure 4b). Thereafter, there is a relatively constant decrease in $N_{obs}(\tau)$ until $\tau = 12$ min. More than 97% of events are at durations of $\tau \leq 12$ min. For the remainder of the distribution, $N_{obs}(\tau)$ is at a level of tens if not single observations. Despite the event duration extending up to τ_{hole} ~48 min, long lasting events number only a few observations. After reducing the distribution to only show events at an altitude of $h \leq 1300$ km (green part of distribution), one can see that events are removed from bins across the entirety of the distribution, and, in particular, electron holes with duration $\tau > 15$ min have been reduced to a maximum of only single digit observations.

The electron hole width, w, distribution (Figure 4c) largely resembles that of the electron hole duration. The maximum number of electron hole observations per width bin is $N_{obs}(w) = 1211$ and occurs at $w = 100$–200 km and then gradually reduces as the width increases. By $w = 3000$ km the observations number less than 20 and are frequently at single digit observations. Similar to the duration distribution, the reduction to events at altitudes of $h \leq 1300$ km (green part of distribution) removes events from bins across the entirety of the width distribution.

Finally, the distribution showing the depth, Δ, of the electron holes (Figure 4d) mostly consists of a single trend. The maximum number of electron hole observations per depth bin is $N_{obs}(\Delta) = 1710$ and occurs at $\Delta = 0.5$–0.55. Thereafter, the observations per bin steadily reduce and eventually number at $N_{obs}(\Delta) < 20$ for $\Delta > 1.9$. Reducing to events at altitudes of $h \leq 1300$ km (green part of distribution) tends to remove events from across the distribution.

A common observation between the bottom three distributions presented in Figure 4 is that the full distributions (green and blue) all cover a wide range of values. Considering only events where the altitude is below 1300 km (the altitude at which the altitude distribution changes its rate of decrease, Figure 4a) removes events from across the full range of all subsequent distributions (Figures 4b–4d).

In order to identify any relationships between the altitude, width, and depth of the events, we present scatterplots in Figures 5 and 6. Both figures show electron hole distributions in terms of altitude-depth (Figures 5a, 5c, 6a, 6c, and 6e) and width-depth (Figures 5b, 5d, 6b, 6d, and 6f) parameter space. Figure 5 further separates events into distributions that are located postterminator ($X_{MSO} < 0\ R_M$; Figures 5a and 5b, blue circles) and preterminator ($X_{MSO} \geq 0\ R_M$; Figures 5c and 5d, red circles), whereas Figure 6 separates events into distributions that are in different solar zenith angle bands (SZA or χ). It is important to note that all events are within illuminated regions of space; and therefore, different ranges of zenith angles represent different levels of solar illumination. Figures 6a and 6b show events that would be most illuminated, $\chi < 75°$ (red circles), Figures 6c and 6d events situated around the terminator, $75° \leq \chi < 120°$ (green circles), and Figures 6e and 6f events that are least illuminated $\chi \geq 120°$ (blue circles). Superimposed on the panels that include altitude is a solid horizontal black line at $h = 1300$ km, the point in Figure 4a where the altitude distribution changes shape (see above).

The distribution of events located preterminator (X_{MSO} positive, Figures 5c and 5d) matches those that are most illuminated ($\chi < 75°$, Figures 6a and 6b). These events are distributed wholly below altitudes of 1300 km and, for the most part, have depths both smaller in size and spread (most below $\Delta = 1.5$). However, the width of these events covers the full distribution seen in Figure 4c. The distribution of events located postterminator (X_{MSO} negative, Figures 5a and 5b) shows two populations, one at altitudes greater than 1000 km where, in general, the range of depths is small ($\Delta = 0.5$–1), and another at altitudes less than 1000 km with depths spreading across the full range observed. For this latter population, in general, as the altitude decreases, the total range of depths increases. The higher-altitude population can be seen to mostly correspond to the least illuminated events ($\chi \geq 120°$, Figures 6e and 6f), whereas the lower altitude population mostly corresponds to events around the terminator region ($75° \leq \chi < 120°$, Figures 6c and 6d), with a subset of the most illuminated events (Figures 6a and 6b). We would expect there to be few low altitude events at the highest zenith angles, otherwise they would be in unilluminated space. The width of an event appears
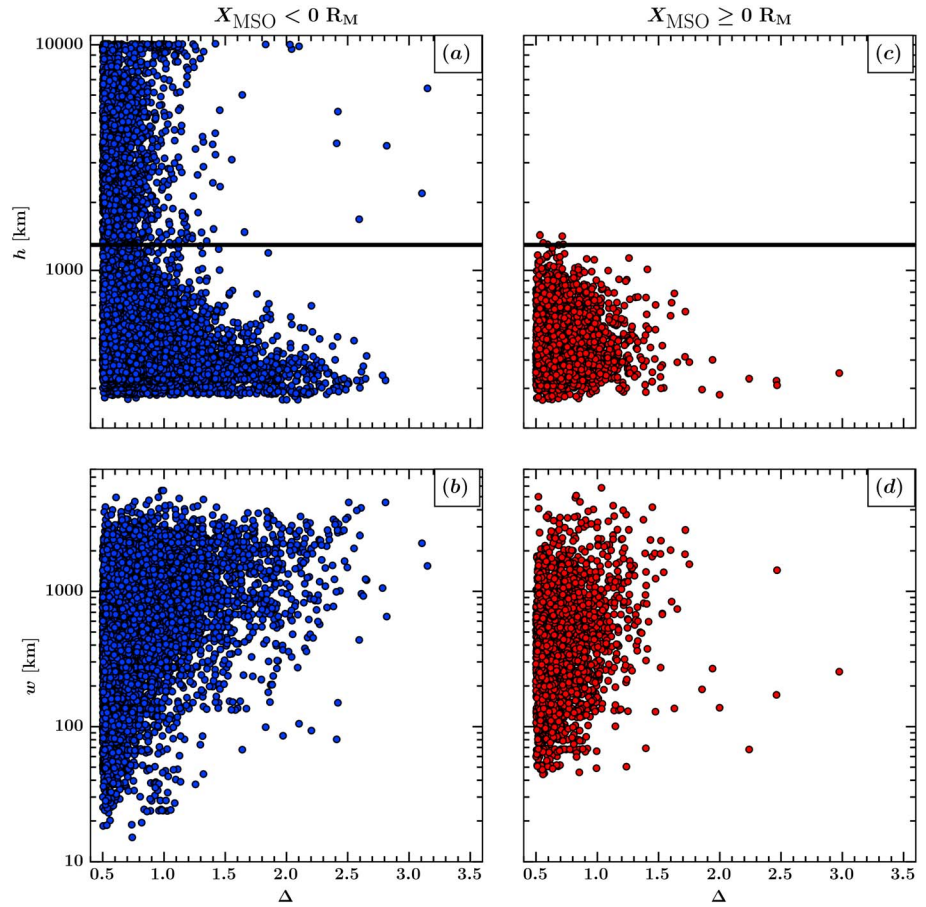
Figure 5. Electron hole altitude, width, and depth scatterplots separated by X_{MSO} position. (a, b) Events grouped in terms of antisunward ($-X_{MSO}$, blue circles) location. (c, d) Events grouped in terms of sunward ($+X_{MSO}$, red circles) location. Figures 5a and 5c show the scatter distribution in altitude and depth parameter space, whereas Figures 5b and 5d are for width and depth parameter space, respectively.

uncorrelated with the locations we have singled out, with all respective panels of Figures 5 and 6 showing events across the full range of widths seen in Figure 4c. However, for the events around the terminator region (Figures 6c and 6d) we see that the largest event depths are reached only at the largest width, which also correspond to a subset of the lowest-altitude events. It is also worth noting that this particular population is only seen when X_{MSO} is negative; thus, the deepest and widest events must occupy a range of $\chi = 90°$–$120°$ within the terminator region (since $\chi > 90°$ for negative X_{MSO}).

As seen in Figure 4, for altitudes $h \leq 1300$ km the electron hole distribution is a continuous distribution with no breaks (Figure 4a). These lower altitude events are distributed across the full width of the subsequent distributions (Figures 4b–4d). In addition, the altitude/depth scatterplots (Figures 5a, 5c, 6a, 6c, and 6e) also presented two distributions that depend on altitude (above and below 1000 km). Since events in the lower altitude regime ($h \leq 1300$ km) make up approximately 80% of the total number of identified events, we choose to focus on them throughout the remainder of the results section.

3.2. Electron Hole Altitude Distribution With Respect to X_{MSO}

The number of orbits, N_{orb}, below 1300 km altitude is presented in Figure 7a, the number of identified electron holes, N_{holes}, in Figure 7b, and the normalized electron hole occurrence, $N_{norm} = N_{holes}/N_{orb}$, for $N_{orb} > 120$ orbits, in Figure 7c, all in an altitude X_{MSO} frame. In Figures 7a–7c, the total number of orbits, electron holes, and normalized occurrence have been grouped into spatial bins of size 50 km (~1.5% R_M) in X_{MSO} and 25 km in altitude. In Figure 7c, normalization of N_{hole} was completed for bins in which $N_{orb} > 120$ orbits in
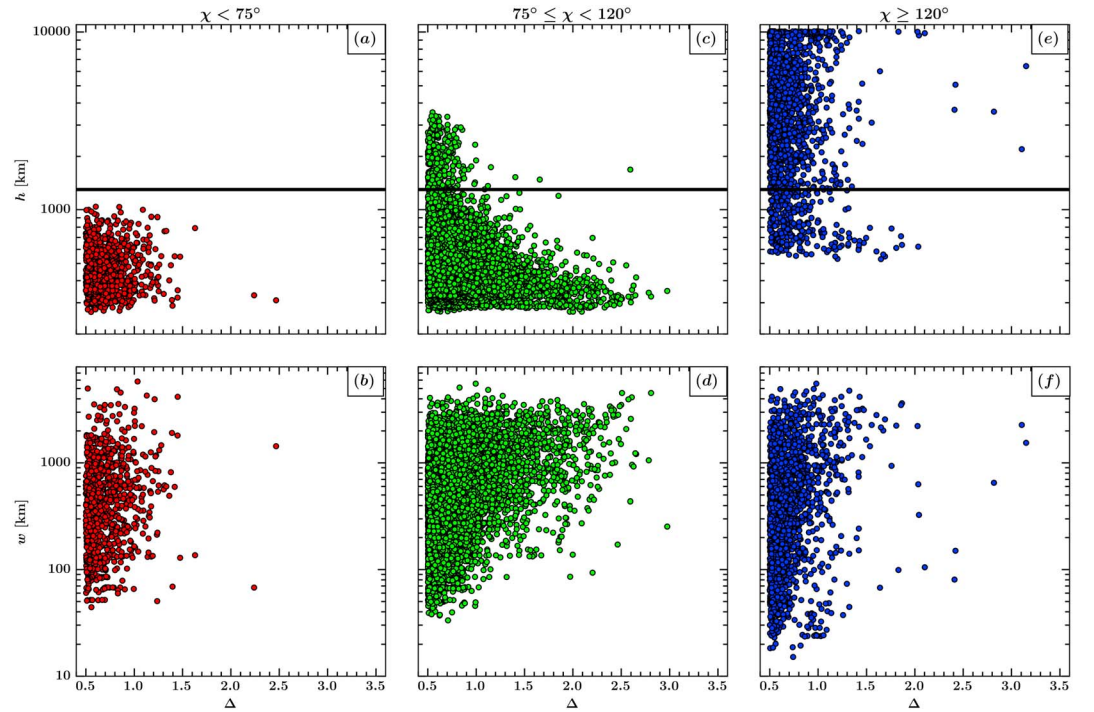
Figure 6. Electron hole altitude, width, and depth scatterplots separated by solar zenith angle (χ) position. (a, b) Events grouped into low zeniths representing high solar illumination ($\chi < 75°$, red circles). (c, d) Events grouped into terminator zeniths ($75° \leq \chi < 120°$, green circles). (e, f) Events grouped into high zeniths representing the lowest solar illumination ($\chi \geq 120°$, blue circles). Figures 6a, 6c, and 6e show scatter distribution in altitude and depth parameter space, whereas Figures 6b, 6d, and 6e are for width, depth parameter space, respectively.

order to reduce false peaks where very few electron holes exist at the same time as very low coverage. For Figures 7a–7c, a region that is white corresponds to null coverage or detection of electron holes.

In Figure 7a, the MEX orbital coverage extends to higher altitudes in the negative X_{MSO} direction than the positive X_{MSO} direction. In this coordinate frame, there is approximately a 4% bias in coverage toward the sunward direction ($N_{orb,tot}(-X_{MSO})/N_{orb,tot}(+X_{MSO}) \sim 0.96$). At altitudes of $h < 600$ km, where the density of orbits is largest (in general, $N_{orb} > 300$), MEX covers a larger range of X_{MSO} in the positive direction than the negative. This is due to our study reducing the data set to that within the illuminated IM. Despite this, for altitudes $h < 600$ km, there is approximately equal coverage either side of the terminator ($N_{orb,tot}(-X_{MSO})/N_{orb,tot}(+X_{MSO}) \sim 1.0$ for $h < 600$ km).

In Figure 7b, low to moderate electron hole occurrences ($1 \leq N_{hole} < 10$, purple-blue-green) are, in general, spread across all regions covered by the MEX orbits. However, for high occurrence ($N_{hole} > 10$, yellow-red), electron holes are identified entirely in spatial bins within the negative X_{MSO} direction and located predominantly toward low altitudes ($h < 500$ km). Compared with holes identified in the positive X_{MSO} direction, there are 2.3 times as many in the negative X_{MSO} direction across the altitude range of $h = 600–1300$ km and 2.5 times as many for altitudes less than 600 km.

Normalization of electron hole occurrence by the number of MEX orbits for bins where $N_{orb} > 120$ (Figure 7c) further highlights the negative X_{MSO} predominance of electron hole identification. N_{norm} gives the probability of an event occurring within each bin of the coordinate frame. There is a region at $X_{MSO} < -0.1 R_M$ and $h < 400$ km, where the likelihood of an electron hole occurring within each bin ranges between 4 and 19%, with the occurrence increasing with decreasing altitude. For the remaining postterminator (negative X_{MSO}) altitudes, the normalized occurrence is generally 1–4% but does reduce to less than 1% at high altitudes. For the vast majority of preterminator (positive X_{MSO}) altitudes, the normalized occurrence is below 1% and, in places, is below 0.2%. We note that for spatial bins at larger positive X_{MSO}, the normalized occurrence increases. This is likely an artifact of lower orbital coverage in this region. Overall, the electron holes are
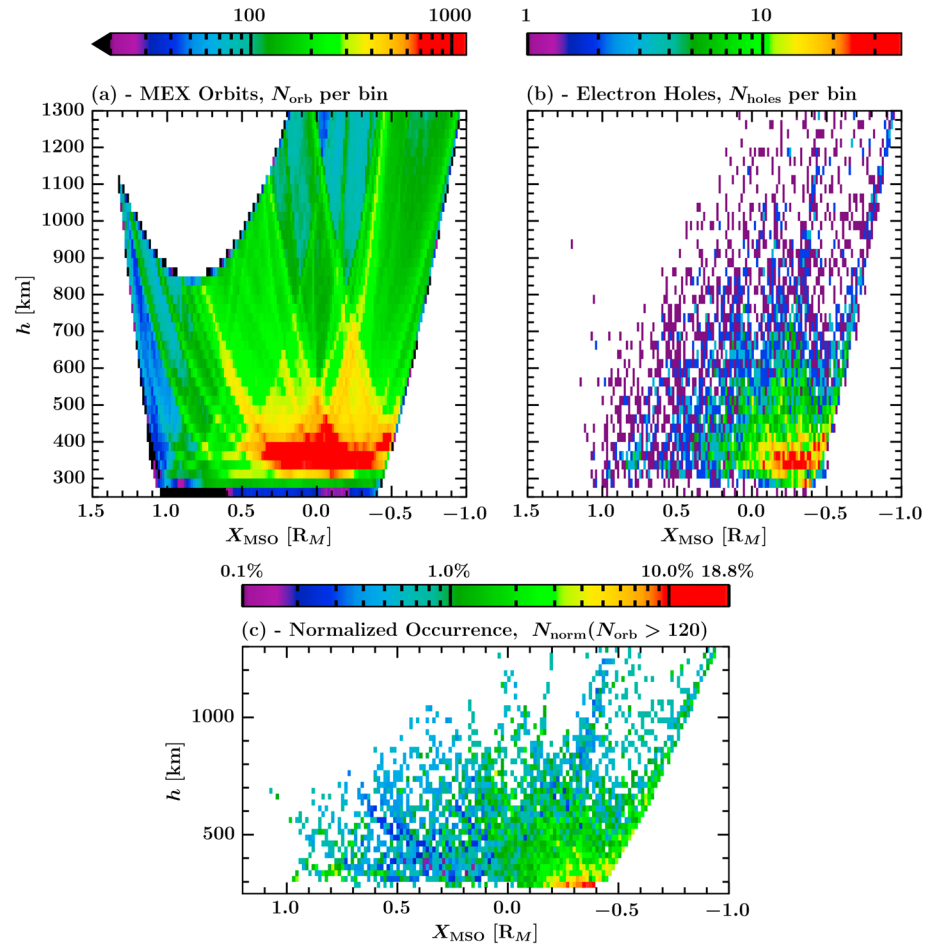
Figure 7. Distribution of electron holes in altitude ($h < 1300$ km) with respect to the Sun-Mars line (X_{MSO}). (a) Orbital coverage of MEX in terms of number of orbits per bin, N_{orb}. (b) Electron hole distribution in terms of number of identified electron holes per bin, N_{hole}. (c) Normalized electron hole occurrence, $N_{norm} = N_{hole}/N_{orb}$ for bins in which $N_{orb} > 120$, given in terms of a percentage occurrence. In each panel, a bin size of 25 km × 50 km in $X_{MSO} \times h$ is used.

identified across a large range of X_{MSO} values and altitudes, but regions in which events occur more predominantly are situated toward low altitudes ($h < 500$ km) in the negative X_{MSO} direction of Mars.

3.3. Distribution of Electron Holes Over the Martian Surface

In Figure 8, we present maps of the distribution of the electron holes, N_{hole} (Figure 8a), the number of MEX orbits, N_{orb} (Figure 8b), the normalized electron hole occurrence, $N_{norm} = N_{hole}/N_{orb}$ (Figure 8c), and the *Cain et al.* [2003] model crustal magnetic field magnitude at an altitude of $h = 300$ km above the surface of Mars (Figure 8d), all in the coordinate frame of latitude, φ, and east longitude, λ_E. To emphasize large-scale occurrences and reduce noise, a spatial resolution of 15 × 15° latitude and east longitude was used. The maps are also divided into three east longitudinal bands, given by $\lambda_1 = 0$–120°, $\lambda_2 = 240$–360°, and $\lambda_3 = 240$–360°, with the boundaries of each superimposed as solid vertical red lines in each panel.

If more than one electron hole exists per orbit per spatial bin, only a single electron hole is counted for that orbit. In Figure 8a, we see moderate electron hole occurrence ($32 < N_{hole} < 46$, green colors) across northern and equatorial latitudes ($\varphi > 30$ N and $\varphi = 30$°S–30°N, respectively) of λ_1, southern ($\varphi < 30$°S) and equatorial latitudes of λ_2, and, albeit more isolated, instances across southern, equatorial, and northern latitudes of λ_3. An aligned structure of high electron hole occurrence ($N_{hole} > 46$, yellow-red) is present across longitudes of $\lambda_E = 150$°–195° at latitudes of $\varphi = 60$°S–75°S. Other regions of high electron hole occurrence are at equatorial latitudes of λ_1 and λ_2, and southern latitudes of λ_3, with all regions having moderate occurrence
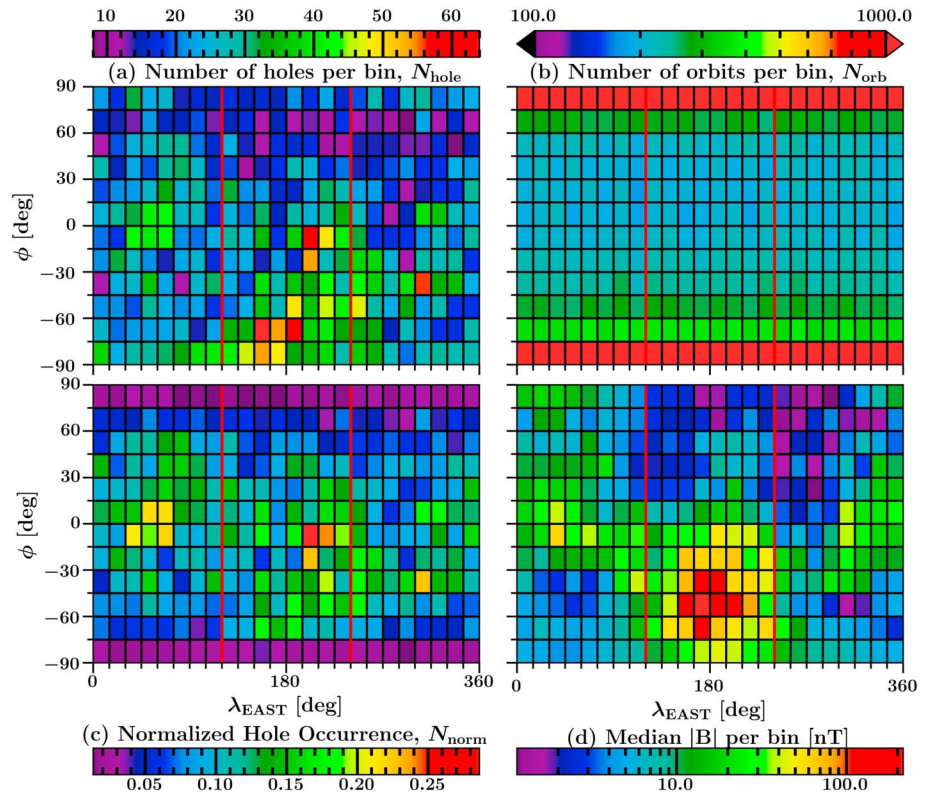
Figure 8. Normalized distribution of identified electron holes at altitudes less than 1300 km above the surface of Mars. Four panels are presented within this figure, each map with a spatial resolution of $15 \times 15°$ latitude (φ) and east longitude (λ_E). (a) Number of electron holes per bin, N_{hole}, with only one event per orbit per bin counted. (b) MEX orbital coverage from 9 February 2004 to 9 May 2014 for segments of orbits within the illuminated IM and at altitudes less than 1300 km, given in terms of number of orbits per bin, N_{orb}. (c) Electron hole occurrence normalized by orbital coverage, N_{norm}, where $N_{norm} = N_{hole}/N_{orb}$. (d) *Cain et al.* [2003] model crustal field magnitude at an altitude of 300 km. Presented as the median crustal field magnitude calculated within each bin, $\widetilde{\boldsymbol{B}} = (b_x + b_y + b_z)^{1/2}$. Solid vertical red lines are superimposed across each panel denoting the equal east longitude bands of 0°–120°, 120°–240°, and 240°–360°, used in the text to describe the observations.

surrounding them. Low electron hole occurrence ($N_{hole} < 32$, purple-blue) forms what appears to be a background level, filling the rest of the spatial bins across the surface of Mars, and being most prevalent across the Northern Hemisphere.

For altitudes less than 1300 km within the illuminated IM, the MEX orbital coverage over the surface of Mars is in excess of 181 orbits per bin (Figure 8b). There is a general orbital bias toward the Southern Hemisphere, with the coverage being at its lowest across equatorial latitudes, and increasing toward both poles where coverage is the highest. Coverage is in excess of 1444 orbits per bin at the southern pole and 1057 orbits per bin at the northern pole. The high coverage at the poles is due to the orbital nature of MEX.

The normalized electron hole occurrence map, Figure 8c, shows the distribution of events unbiased by MEX coverage. Here the fractional percentage of orbits in which at least one event was detected is presented and can be considered a form of probability indicator of electron hole occurrence across the study period. A clear pattern is formed in regions where $N_{norm} > 0.11$. This occurs around the equator at all longitudes and is also distributed toward the Northern Hemisphere in λ_1, the Southern Hemisphere in λ_2, the Southern Hemisphere at low longitudes within λ_3, and spread around the equator at high longitudes within λ_3. Breaks in the $N_{norm} > 0.11$ occurrence pattern are seen when the normalized occurrence reduces below $N_{norm} = 0.11$ and then returns back to $N_{norm} > 0.11$. This is seen at low equatorial latitudes of λ_2 and across almost all latitudes for central longitudes within λ_3 ($270° < \lambda < 285°$). In general, there is a background level of $N_{norm} \leq 0.08$ present across the entire map. Despite the electron hole occurrence map (Figure 8a) presenting instances of moderate to high occurrence ($N_{hole} > 32$) at polar latitudes of both hemispheres, for the most part, the

corresponding normalized occurrence is incredibly low ($N_{norm} \leq 0.04$). From this map it is thus clear that the events do occur predominantly over particular regions of the Martian surface.

The crustal magnetic field map in Figure 8d was produced from the *Cain et al.* [2003] model. This model is derived from in situ measurements taken by the MAG/ER instruments [*Acuña et al.*, 1992] on board the MGS mission. *Cain et al.* [2003] noted that at the lowest MGS altitudes ($h < 200$ km), the model could have an error as large as 20 nT. The map of Figure 8d was produced for an altitude of $h = 300$ km, where the errors should be somewhat lower, and at the very least can be used as a general idea of the crustal field distribution. Within each $15 \times 15°$ spatial bin, the median model magnetic field magnitude, $\widetilde{B} = (b_x{}^2 + b_y{}^2 + b_z{}^2)^{1/2}$, was calculated to match the spatial resolution of the other panels in Figure 8.

For normalized occurrence of $N_{norm} > 0.11$, the electron hole distribution in Figure 8c shows a resemblance to the pattern formed by moderate-high strength crustal magnetic fields ($10 < \widetilde{B} < 70$ nT, green-yellow in Figure 8d). The features in normalized occurrence seen in Figure 8c such as the population starting around equatorial latitudes and extending toward the North within λ_1, the general tendency of being higher within the Southern Hemisphere of λ_2 and the population shifting from the Southern Hemisphere at low longitudes to equatorial latitudes at high longitudes (along with a reduction in between at around $\lambda_E = 270°$) within λ_3 all match the behavior of the model crustal magnetic field magnitude in Figure 8d. However, we also see regions in which the two do not match as well. The most significant are at northern polar latitudes of λ_1 and low equatorial latitudes of λ_2 (i.e., 15°S–30°S) where the model crustal magnetic fields tend toward their largest values. It was noted above that there is a reduction in normalized occurrence within this latter region, although the reduction is surrounded by moderate to high normalized occurrence. In general, we also see that where the model crustal fields are their strongest, we tend to have lower normalized occurrence compared to surrounding bins. Despite the overall similarities between the electron hole normalized occurrence and *Cain et al.* [2003] model crustal magnetic field (Figures 8c and 8d) maps, the aforementioned differences could suggest that it is not only the magnetic field magnitude controlling the occurrence, as will be discussed later in this paper.

3.4. Altitudinal Distribution of Electron Holes Above Crustal Fields

In Figure 9 we present the altitude distribution of events above the surface of Mars, grouped into specific regions of crustal magnetic fields. Figures 9a–9c present observations grouped into three east longitudinal bands of $\lambda_1 = 0°–120°$ (Figure 9a), $\lambda_2 = 120°–240°$ (Figure 9b), and $\lambda_3 = 240°–360°$ (Figure 9c). Each of these three panels is presented as a set of two subpanels. The top subpanel presents the normalized electron hole occurrence, N_{norm}, as a function of latitude, φ, and altitude, h, with bins of size 50 km altitude and 10° latitude. The bottom subpanel presents the altitude distribution of electron holes, $N_{obs}(\lambda, \varphi, h)$, after being further grouped into three latitude bands, mid to high northern latitudes ($\varphi_N > 30°$, red), equatorial latitudes ($-30° \leq \varphi_{EQ} \leq 30°$, green), and mid to high southern latitudes ($\varphi_S < -30°$, blue). Also on the bottom subpanel is a vertical solid black line positioned at an altitude of $h = 500$ km. These choices of longitude and latitude bands were chosen to match the description of Figure 8 in section 3.3 and to isolate the areas in which the crustal fields are at their strongest (equatorial and toward the north in λ_1, southern latitudes in λ_2, and primarily equatorial latitudes of λ_3). Figures 9d and 9e show the normalized electron hole occurrence maps (as in Figure 8c) but for events at $h \leq 500$ km and events in the range $500 < h \leq 1300$ km, respectively.

In the top subpanel of Figure 9a, moderate to high normalized electron hole occurrence ($N_{norm} > 6\%$, green-red) is seen preferentially at northern and equatorial latitudes (φ_{EQ} and φ_N), for altitudes $h < 500$ km. There are some isolated pixels of similar occurrence at midsouthern latitudes, but these are confined to even lower altitudes ($h < 300$ km, periapsis at the very beginning of MEX mission). In general, as the altitude increases, the normalized occurrence rapidly reduces, with almost all latitudes having a normalized occurrence of less than 3% by $h = 550$ km. This is further demonstrated in the altitude distributions shown in the bottom subpanel of Figure 9a. Here we see that, at altitudes up to $h = 500$ km, electron hole occurrence is greatest across equatorial latitudes, followed by northern high latitudes (for $h > 300$ km) and then finally southern high latitudes.

In the top subpanel of Figure 9b, we see moderate to high normalized electron hole occurrence preferentially distributed toward equatorial and southern latitudes, and as in Figure 9a, they are at low altitudes ($h < 500$ km). Compared to Figure 9a, the number of events across northern latitudes has reduced, whereas the number of events across southern latitudes has increased. Also of note is that more events
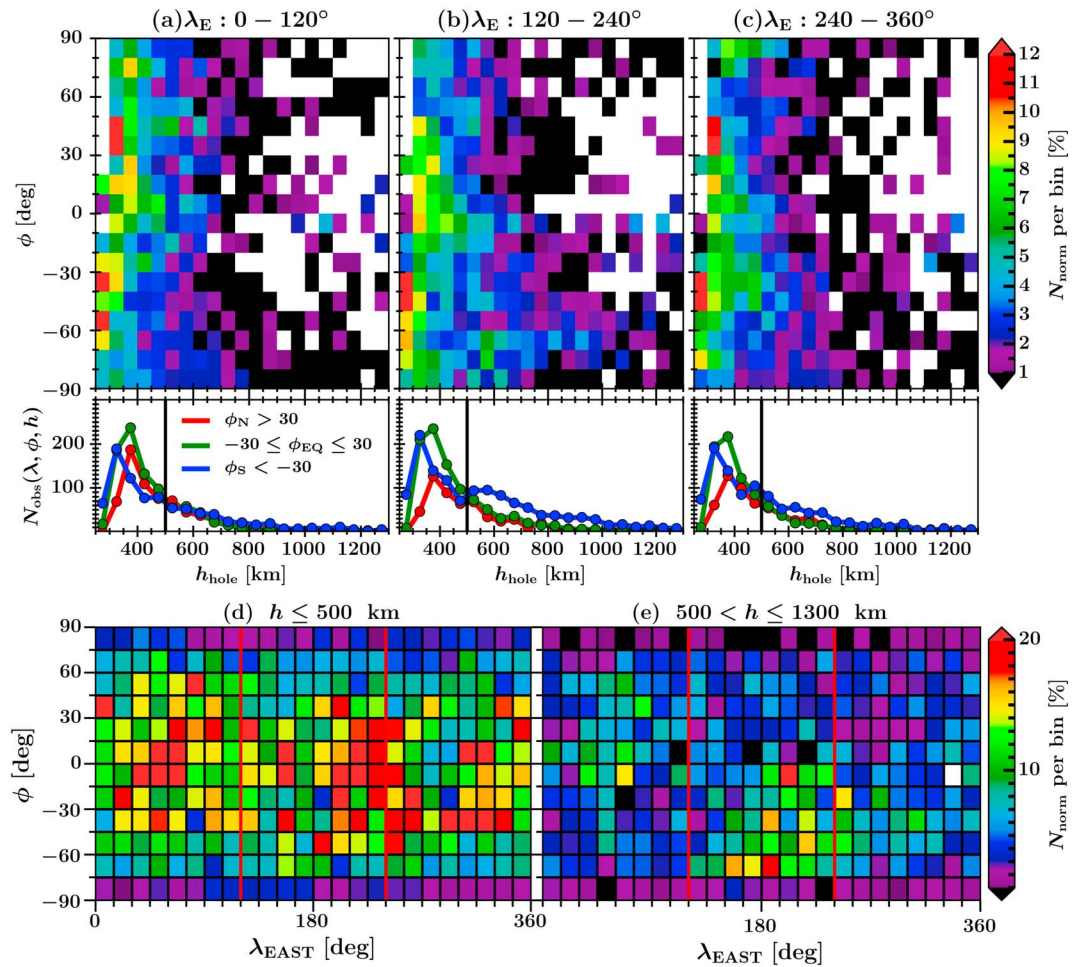
Figure 9. Altitude distribution of electron holes (for altitudes less than 1300 km) above regions in which the crustal magnetic fields have varying predominance. (a–c) Three pairs of subpanels. The top subpanel shows the normalized occurrence of electron holes (N_{norm}) within bins of latitude (φ) and altitude (h). The bin sizes correspond to 10° and 50 km, respectively. The color scale is the same across all top subplots. The bottom subpanels shows the number of observations per altitude bin for all events grouped into three latitude bands. The latitude bands are mid to high northern ($\varphi_N > 30°$, red profile), equatorial (φ_{EQ}: −30° to 30°, green profile), and mid to low southern ($\varphi_S < −30°$, blue profile). Figures 9a–9c represent observations within three east longitude bands: λ_E: 0–120°, where crustal fields are distributed equatorially and toward the north, λ_E: 120–240°, where crustal fields are distributed across the entirety of the Southern Hemisphere and have the highest magnitudes, and λ_E: 240–360°, where crustal fields are distributed toward southern latitudes for low longitude and equatorially for higher longitudes within the band, respectively. (d, e) The spatial distribution of normalized event occurrence, N_{norm}, as was in Figure 8c, but grouped into events below 500 km altitude (Figure 9d) and within 500–1300 km range (Figure 9e).

are observed at higher altitudes, with higher occurrence present up to $h = 1000$ km across southern latitudes of $\varphi \sim 60°S$–$80°S$. The bottom subpanel of Figure 9b mirrors this description, especially in demonstrating the increased number of events across southern latitudes and a large range of altitudes. Also of note is the reduction in occurrence of events across northern latitudes for $h < 500$ km when compared to Figure 9a.

The results shown for electron holes identified in longitude band λ_3 (Figure 9c) resemble those from λ_1 (Figure 9a) and λ_2 (Figure 9b). For lower altitudes, the majority of events are distributed within equatorial latitudes (green profile, bottom subpanel), closely followed by southern latitudes. Similar to λ_1 (Figure 9a), all three observation frequency profiles for each latitude band, as shown in the bottom subpanel, all reduce at similar, and fairly rapid, rates as the altitude increases. However, similar to λ_2 (Figure 9b), the southern latitude profile is enhanced for altitudes greater than 500 km.

In summary, at lower altitudes electron holes are distributed somewhat more homogenously, albeit with higher occurrence situated above longitudes and latitudes where crustal magnetic fields are present (see Figure 8d). As the altitude increases, the occurrence rapidly reduces, with normalized occurrence less than 5% across the majority of latitudes and altitudes. However, where the crustal magnetic fields are at their strongest (southern latitudes of central east longitudes, see Figure 8d), we see enhanced occurrence up to higher altitudes. We further demonstrate this in Figures 9d and 9e. The normalized distribution map of electron holes at $h \leq 500$ km, Figure 9d, shows a fairly homogeneous distribution, albeit still showing similar patterns to the locations of moderate crustal magnetic field magnitudes (Figure 8d). For the normalized distribution map of electron holes at higher altitudes, Figure 9e, we now see the events distributed around regions where the crustal magnetic fields are at their strongest (e.g., southern latitudes at central east longitudes). Aside from this region, and one other at equatorial to northern latitudes at low east longitudes (which is the next most significant region of crustal magnetic fields), the normalized occurrence is, in general, significantly lower. These results suggest a relation between the altitudinal distribution of an electron hole and the intensity of crustal magnetic fields.

4. Discussion

This study has used a proxy measurement of the electron flux derived from the MEX ASPERA-3 ELS electron flux measurements integrated across the 20–200 eV energy range to identify electron holes in the illuminated IM. We have used in excess of 5 Martian years (~10 Earth years) of data to complete an extensive statistical study of such phenomena. This data set has allowed us to complete a study over a significantly longer time period than any other previous study. Using an automated algorithm, electron holes within the illuminated IM have been identified. By only considering the illuminated regions we avoid the plasma voids studied by *Mitchell et al.* [2001], *Soobiah et al.* [2006], *Brain et al.* [2007], and *Steckiewicz et al.* [2015], which were primarily identified within the shadowed region in the tail of the IM. The results presented in this paper can be briefly summarized as follows:

1. The electron holes have been parameterized in terms of their altitude, duration, width, and depth. In general, the electron holes were found to have large ranges in these parameters, but separate populations in altitude with respect to these parameters can be identified (see section 3.1, Figures 4–6).
2. Electron holes at $h \leq 1300$ km are observed to occur in all regions of space with respect to the Martian terminator plane ($X_{MSO} = 0$), although there is a tendency toward occurrence in the negative X_{MSO} direction (see sections 3.1, 3.2, Figures 5–7).
3. The spatial distribution above the Martian surface is related to the crustal magnetic field locations (see section 3.3, Figure 8).
4. The altitude distribution of electron holes shows more events occurring at higher altitudes over regions of larger crustal magnetic field magnitude (see section 3.4, Figure 9).

The above four points will now be discussed in detail. The full altitude distribution (Figure 4a) of electron holes has a spread from 266 to 10117 km (the lower limit is defined by the periapsis of the MEX orbit). However, a clear change in the trend of occurrence frequency was seen at $h = 1300$ km, with ~80% of identified electron holes occurring below this altitude. There are potentially multiple trends seen above $h = 1300$ km, although they are much more similar to each other than the trend at lower altitudes. Since the bulk of the identified events occupy the first trend, this result suggests that the formation conditions and mechanisms of the electron hole phenomena are likely more common closer to the planet's surface rather than further away and, as will be discussed later, are likely related to the crustal magnetic fields. The higher-altitude events were solely distributed across the negative X_{MSO} direction, with the highest-altitude events being located at high solar zenith angles placing them deeper within the induced magnetotail of Mars (Figures 5a, 5c, 6a, 6c, and 6e). The lack of events at high altitudes in the positive X_{MSO} direction is an effect of the MEX orbit and the Mars plasma environment with the boundary to the IM (the MPB) being, on average, at lower altitudes in the positive X_{MSO} direction. Consequently, this limits the maximum altitude at which an electron hole can be identified.

Scatter distributions of the electron hole altitude against depth parameters (Figures 5a, 5c, 6a, 6c, and 6e) further demonstrated different populations as a function of altitude. The depth of an event is a measure of the reduction in the *f* parameter within the hole, and the results demonstrate that events at higher altitudes

tend to have smaller depths. This may indicate the process for producing an electron hole being weaker in the deep magnetotail. In general, low-altitude events, below 1300 km, have a large range of depths, although we also note that the most illuminated ($\chi < 75°$), preterminator (positive X_{MSO}) events tend to have similar depths to the least illuminated ($\chi \geq 120°$), postterminator (negative X_{MSO}) events. Events around the terminator region ($75° \leq \chi < 120°$) were shown to include the largest depths.

Further scatter distributions of the electron hole width against depth (Figures 5b, 5d, 6b, 6d, and 6f) were produced to be able to relate the altitude, depth, and width of the events. The width of an event was calculated by considering the MEX velocity and trajectory across an electron hole and gives a measure of the scale size. Small event depths were shown to correspond to a large range in widths, whereas, as the depth increases, the width tends to increase, and the range of widths decreases. As noted above, the events with the largest depths were found to be around the terminator region and also correspond to the lowest altitudes ($h < 500$ km). The lowest-altitude events around the terminator, therefore, are also the widest and deepest. In general, the range in widths calculated for the electron holes is very large, with events at altitudes less than 1300 km spanning from 44 to 5824 km in width and having a corresponding mean and median averages of 797 and 582 km, respectively. This large range, which almost exceeds the diameter of Mars at the upper end, suggest that the electron holes have a complicated and highly variable geometry in space around the planet, such that MEX passes through these geometries in different ways. If we imagine an electron hole region being an elongated tube-like structure, MEX traveling along the tube would result in a much larger calculated width than if the MEX trajectory cuts across the tube. Understanding the detailed geometry of the electron holes will be left for a later study.

Since we calculated the width of the electron holes via the same method that *Duru et al.* [2011] used for the electron density depressions, we can compare our results. The width distribution of electron density depressions in the Duru et al. study was found to be between 340 km and 3280 km, and on average 950 km. This range is within that found in this study although the minimum and maximum values are somewhat larger and smaller, respectively. Despite this, the Duru et al. average event width of 950 km is similar to the mean width of 797 km found in this study. Note that, as explained in section 1, the Duru et al. electron density depressions are related to the thermal component of the electron plasma population, whereas the electron holes in our study correspond to the superthermal component of the plasma, thus even though they appear to be similar features, they could very well not be.

Relating to the second discussion point, we focus on the distribution of electron holes at altitudes of less than 1300 km (Figures 7 to 9). In Figure 7 we presented the occurrence of events in altitude, X_{MSO} parameter space and found that, despite the events being located throughout a large range of this parameter space, there is a higher likelihood of the electron holes occurring toward lower altitudes ($h < 500$ km) in the negative X_{MSO} direction ($X_{MSO} < -0.1 R_M$) (Figures 7b and 7c). For similar low altitudes, as X_{MSO} becomes more positive, the more rapidly the likelihood of identifying an event decreases (order of magnitude reduction from $X_{MSO} = -0.4$ to $0.2 R_M$). This result shows that the electron holes are predominantly features of the near-planet-induced magnetotail. Despite this, the electron holes do not have insignificant occurrence across the terminator plane ($X_{MSO} = 0$) where the plasma environment and corresponding physical processes can be considerably different.

Moving to the relationship of the holes with the planetary surface, point 3, the spatial distribution of the electron holes across the surface of Mars resembles regions in which the crustal magnetic field magnitude is locally high (Figures 8c and 8d). This spatial distribution leads to the suggestion that the crustal magnetic fields must play an important role in the formation of the electron hole phenomena. It was noted that the event occurrence distribution did not match the crustal field distribution in a few places. One of these was at northern polar latitudes within east longitudes of 0° to 120°. In this region there are moderate crustal magnetic field regions but very low normalized occurrence of electron holes. The reason for this could be related to the MEX orbit, since any passage over a polar region close to the planet (where the crustal fields are significant) is expected to happen quite rapidly, thus an event could be difficult to detect. Another region where the crustal fields and event occurrence failed to match was at low equatorial latitudes of central eastern longitudes (0°–30°S, 150°E–195°E). Once again, this region has moderate to high (larger the farther south) crustal magnetic fields, but a reduction in event occurrence. Along with this, in regions where the crustal fields are most intense, the event occurrence is reduced compared to adjacent regions. This could suggest that it is not

just the magnitude of the crustal magnetic fields that controls the presence of the electron holes (e.g., it could also be related to their orientation and the external solar wind/IMF conditions).

Finally, point 4, at lower altitudes ($h < 500$ km) the bulk of electron holes are distributed more homogenously above regions of crustal magnetic fields (see Figure 9). As the altitude increases, significant occurrence of events is only prominent in the surrounding regions of the most intense crustal magnetic fields (e.g., at the Southern Hemisphere across the central eastern longitudes (120° to 240°)), see Figure 9e. This indicates that higher-altitude events occur close to regions of strong crustal magnetic fields.

Before discussing our results with respect to that of others we first describe the physical manifestation of the electron holes in terms of the electron spectrum. ASPERA-3 ELS measures the superthermal population of electrons in the Mars plasma environment. Thus, the electron holes we describe in this paper are reductions in this superthermal component. The superthermal electrons will originate from an input of energy into the IM, and such a source is likely from the interaction of the solar wind and IMF with the Martian plasma environment. If no crustal magnetic fields are present, then the IMF can reach low altitudes, draping around (and into) the ionosphere of Mars. Previous studies by *Mitchell et al.* [2001] and *Brain et al.* [2003] noted that the crustal magnetic fields of Mars have an important role at altitudes up to 1000 km in the interaction of the Martian atmosphere and upper ionosphere with the solar wind. Thus, if crustal magnetic fields are present, the IMF can be held off to higher altitudes creating so-called mini-magnetospheres [*Harnett and Winglee*, 2003; *Brain et al.*, 2005; *Dubinin et al.*, 2007, 2008; *Fränz et al.*, 2006]. At the outer layers of these mini-magnetospheres, reconnection events may occur between the crustal fields and IMF leading to a method of input of the solar wind/magnetosheath into the IM and a removal of atmospheric electrons out from the IM. In such interaction regions, inner layers may be closed-off to the IMF. An electron hole could then either be a region in which a reconnection event has occurred and evacuated the superthermal population or, alternatively, a region that has not been connected to the IMF for a significant amount of time (i.e., the inner layers of the mini-magnetospheres), such that any superthermal component has been lost through absorption into the atmosphere or diffusion away from the planet.

The previous studies of *Mitchell et al.* [2001], *Soobiah et al.* [2006], *Brain et al.* [2007], and *Steckiewicz et al.* [2015] all have similar interpretations to this. *Mitchell et al.* [2001] proposed that it is the magnetic topology that is restricting solar wind flow into the magnetotail. Similarly, the pitch angle distribution study by *Brain et al.* [2007] suggested that the topology of plasma voids is such that the crustal fields are closed field regions. In this case the plasma voids would manifest in the nightside since loss processes (e.g., atmospheric absorption) would dominate source processes, hence removing the superthermal component. The *Soobiah et al.* [2006] study instead suggested the voids may be due to the crustal magnetic fields being connected to the IMF, allowing an atmospheric escape channel. The *Steckiewicz et al.* [2015] study, although lacking coverage over the strongest regions of crustal magnetic fields, found that superthermal electron depletions became distributed above crustal fields at altitudes above 170 km, whereas below this they were homogeneously spread above the surface. This lower altitude distribution was suggested to be due to electron absorption by atmospheric CO_2. All of these studies focused on electron depletions observed within the optical shadow of Mars.

Comparing the results of our study to those above, we first note that the identification algorithm was designed to identify only electron depletions outside of the optical shadow. We suggest that the events we identify at lower altitudes, which are distributed more evenly above crustal fields, could represent the distribution seen for closed magnetic topology regions. The higher-altitude events are distributed closer to the strongest crustal field regions, with normalized occurrence highest adjacent to the most intense regions (Figure 9e). This distribution could be related to regions where the formation is due to interactions of the crustal fields with the IMF. However, without a method, or the instrumentation for identifying the magnetic topology, this cannot be confirmed.

The aim of this study did not directly concern itself with the identification of the formation mechanisms of electron holes but to identify locations in which they are more likely to occur such that further studies can look into the conditions required for an electron hole to be present. To do this, a similar in-depth study could be carried out on just the optical shadow region of Mars. Such results could be directly compared to those discussed in the previous paragraphs. In addition to this, now that MAVEN is continuously sampling the Martian plasma environment, it will soon have a fuller coverage across the entire surface of the planet.

Further studies could then be completed to understand these phenomena in terms of their magnetic topology over extended altitude ranges never before possible.

5. Conclusions

We observe rapid reductions in a proxy measurement of electron flux, referred to as electron holes, that occur within the illuminated Martian IM. We have presented a detailed survey of these phenomena from proxy measurements of the electron flux obtained by the ASPERA-3 ELS instrument on board the MEX spacecraft. The study was completed across a period exceeding 5 Martian years (~10 Earth years) from 9 February 2004 to 9 May 2014. We conclude that the electron holes are observed within 56% of orbits across this study period, falling predominantly at altitudes less than 1300 km and at solar zenith angles between 90° and 120°. The distribution of these events above the surface of Mars was observed to bear close resemblance to that of the locations of crustal magnetic fields as predicted by the *Cain et al.* [2003] model. Additionally, the altitudinal distribution of events was observed to relate to the local intensity of magnetic fields (e.g., increased occurrence at higher altitudes where the crustal fields are most intense). This suggests that these phenomena are a feature of the solar wind-Martian plasma system interaction. Further characterization of the mechanisms and processes involved in the electron hole regions may give further insight into atmospheric loss processes seen at Mars.

References

Acton, C. H. (1996), Ancillary Data Services of NASA's Navigation and Ancillary Information Facility, *Planet. Space Sci.*, *44*(1), 65–70, doi:10.1016/0032-0633(95)00107-7.

Acuña, M. H., et al. (1992), Mars Observer magnetic fields investigation, *J. Geophys. Res.*, *97*(E5), 7799–7814, doi:10.1029/92JE00344.

Acuña, M. H., et al. (1998), Magnetic field and plasma observations at Mars: Initial results of the Mars Global Surveyor mission, *Science*, *279*(5357), 1676–1680, doi:10.1126/science.279.5357.1676.

Acuña, M. H., et al. (1999), Global distribution of crustal magnetization discovered by the Mars Global Surveyor MAG/ER experiment, *Science*, *284*(5415), 790–793, doi:10.1126/science.284.5415.790.

Acuña, M. H., et al. (2001), Magnetic field of Mars: Summary of results from the aerobraking and mapping orbits, *J. Geophys. Res.*, *106*(E10), 23,403–23,418, doi:10.1029/2000JE001404.

Andrews, D. J., H. J. Opgenoorth, N. J. T. Edberg, M. André, M. Fränz, E. Dubinin, F. Duru, D. Morgan, and O. Witasse (2013), Determination of local plasma densities with the MARSIS radar: Asymmetries in the high-altitude Martian ionosphere, *J. Geophys. Res. Space Physics*, *118*, 6188–6196, doi:10.1002/jgra.50593.

Andrews, D. J., M. André, H. J. Opgenoorth, N. J. T. Edberg, C. Diéval, F. Duru, D. A. Gurnett, D. Morgan, and O. Witasse (2014), Oblique reflections in the Mars Express MARSIS data set: Stable density structures in the Martian ionosphere, *J. Geophys. Res. Space Physics*, *119*, 3944–3960, doi:10.1002/2013JA019697.

Barabash, S., et al. (2004), *ASPERA-3: Analyser of Space Plasmas and Energetic Ions for Mars Express*, pp. 121–140 , European Space Agency Publication Division, Noordwijk, Netherland, SP-1240.

Barabash, S., et al. (2006), The Analyzer of Space Plasmas and Energetic Atoms (ASPERA-3) for the Mars Express mission, *Space Sci. Rev.*, *126*(1-4), 113–164, doi:10.1007/s11214-006-9124-8.

Brace, L. H., R. F. Theis, H. G. Mayr, S. A. Curtis, and J. G. Luhmann (1982), Holes in the nightside ionosphere of Venus, *J. Geophys. Res.*, *87*, 199–211, doi:10.1029/JA087iA01p00199.

Brain, D. A., F. Bagenal, M. H. Acuña, and J. E. P. Connerney (2003), Martian magnetic morphology: Contributions from the solar wind and crust, *J. Geophys. Res.*, *108*(A12), 1424, doi:10.1029/2002JA009482.

Brain, D. A., J. S. Halekas, R. Lillis, D. L. Mitchell, R. P. Lin, and D. H. Crider (2005), Variability of the altitude of the Martian sheath, *Geophys. Res. Lett.*, *32*, L18203, doi:10.1029/2005GL023126.

Brain, D. A., R. J. Lillis, D. L. Mitchell, J. S. Halekas, and R. P. Lin (2007), Electron pitch angle distributions as indicators of magnetic field topology near Mars, *J. Geophys. Res.*, *112*, A09201, doi:10.1029/2007JA012435.

Cain, J. C., B. B. Ferguson, and D. Mozzoni (2003), An *n* = 90 internal potential function of the Martian crustal magnetic field, *J. Geophys. Res.*, *108*(E2), 5008, doi:10.1029/2000JE001487.

Chicarro, A., P. Martin, and R. Traunter (2004), *Mars Express: A European Mission to the Red Planet*, pp. 3–16 , European Space Agency Publication Division, Noordwijk, Netherlands, SP-1240.

Cloutier, P. A., et al. (1999), Venus-like interaction of the solar wind with Mars, *Geophys. Res. Lett.*, *26*(17), 2685–2688, doi:10.1029/1999GL900591.

Collinson, G. A., et al. (2014), The extension of ionospheric holes into the tail of Venus, *J. Geophys. Res. Space Physics*, *119*, 6940–6953, doi:10.1002/2014JA019851.

Dubinin E., M. Fränz, J. Woch, E. Roussos, S. Barabash, R. Lundin, J. D. Winningham, R. A. Frahm, and M. Acuña (2007), Plasma morphology at Mars. ASPERA-3 observations, in *The Mars Plasma Environment*, edited by C. T. Russell, pp 209–238, Springer, New York, doi:10.1007/978-0-387-70943-7_8.

Dubinin, E., M. Fraenz, J. Woch, R. Modolo, G. Chanteur, F. Duru, D. A. Gurnett, S. Barabash, and R. Lundin (2012), Upper ionosphere of Mars is not axially symmetrical, *Earth Planets Space*, *64*(2), 113–120, doi:10.5047/eps.2011.05.022.

Dubinin, E. M., M. Fraenz, J. Woch, E. Roussos, J. D. Winningham, R. A. Frahm, A. Coates, F. Leblanc, R. Lundin, and S. Barabash (2008), Access of solar wind electrons into the Martian magnetosphere, *Ann. Geophys.*, *26*, 3511–3524, doi:10.5194/angeo-26-3511-2008.

Duru, F., D. A. Gurnett, D. D. Morgan, J. D. Winningham, R. A. Frahm, and A. F. Nagy (2011), Nightside ionosphere of Mars studied with local electron densities: A general overview and electron density depressions, *J. Geophys. Res.*, *116*, A10316, doi:10.1029/2011JA016835.

Edberg, N. J. T., M. Lester, S. W. H. Cowley, and A. I. Eriksson (2008), Statistical analysis of the location of the Martian magnetic pileup boundary and bow shock and the influence of crustal magnetic fields, *J. Geophys. Res.*, *113*, A08206, doi:10.1029/2008JA013096.

Frahm, R. A., et al. (2006), Carbon dioxide photoelectron energy peaks at Mars, *Icarus*, *182*(2), 371–382, doi:10.1016/j.icarus.2006.01.014.

Fränz, M., et al. (2006), Plasma intrusion above Mars crustal fields—Mars Express ASPERA-3 observations, *Icarus*, *182*(2), 406–412, doi:10.1016/j.icarus.2005.11.016.

Fränz, M., E. Dubinin, E. Roussos, J. Woch, J. D. Winningham, R. Frahm, A. J. Coates, A. Fedorov, S. Barabash, and R. Lundin (2007), Plasma moments in the environment of Mars, *Space Sci. Rev.*, *126*(1-4), 165–207, doi:10.1007/s11214-006-9115-9.

Furman, M. A., and M. T. F. Pivi (2002), Probabilistic model for the simulation of secondary electron emission, *Phys. Rev. ST Accel. Beams*, *5*, 12, doi:10.1103/PhysRevSTAB.5.124404.

Harnett, E. M., and R. M. Winglee (2003), The influence of a mini-magnetopause on the magnetic pileup boundary at Mars, *Geophys. Res. Lett.*, *30*, 2074, doi:10.1029/2003GL017852.

Jakosky, B., et al. (2015), The Mars Atmosphere and Volatile Evolution (MAVEN) mission, *Space Sci. Rev.*, *195*(1-4), 3–48, doi:10.1007/s11214-015-0139-x.

Lundin, R., S. Barabash, M. Yamauchi, H. Nilsson, and D. Brain (2011), On the relation between plasma escape and the Martian crustal magnetic field, *Geophys. Res. Lett.*, *38*, L02102, doi:10.1029/2010GL046019.

Mitchell, D. L., R. P. Lin, C. Mazelle, H. Rème, P. A. Cloutier, J. E. P. Connerney, M. H. Acuña, and N. F. Ness (2001), Probing Mars' crustal magnetic field and ionosphere with the MGS Electron Reflectometer, *J. Geophys. Res.*, *106*(E10), 23,419–23,428, doi:10.1029/2000JE001435.

Nilsson, H., N. J. T. Edberg, G. Stenberg, S. Barabash, M. Holmström, Y. Futaana, R. Lundin, and A. Fedorov (2011), Heavy ion escape from Mars, influence from solar wind conditions and crustal magnetic fields, *Icarus*, *215*(2), 475–484, doi:10.1016/j.icarus.2011.08.003.

Pérez-de-Tejada, H. (2004), Plasma channels and electron density profiles near the midnight plane in the Venus nightside ionosphere, *J. Geophys. Res.*, *109*, A04106, doi:10.1029/2002JA009811.

Pischel, R., and T. Zegers (2009), Mars Express science planning and operations, in *Mars Express: The Scientific Investigations*, pp. 249–256 , ESA Communication Production Office, Noordwijk, Netherlands, SP-1291.

Soobiah, Y., et al. (2006), Observations of magnetic anomaly signatures in Mars Express ASPERA-3 ELS data, *Icarus*, *182*(2), 396–405, doi:10.1016/j.icarus.2005.10.034.

Steckiewicz, M., et al. (2015), Altitude dependence of nightside Martian suprathermal electron depletions as revealed by MAVEN observations, *Geophys. Res. Lett.*, *42*, 8877–8884, doi:10.1002/2015GL065257.

Zender, J. F., et al (2009), Spacecraft and payload data handling, in *Mars Express: The Scientific Investigations*, pp. 257–278 , ESA Communication Production Office, Noordwijk, Netherlands, SP-1291.